UNIVERSIDADE DE SÃO PAULO

INSTITUTO DE QUÍMICA

Graduate Program in Chemistry

VITOR RENATO RIBEIRO SILVEIRA

Gold and Gold-Palladium Branched Nanocrystals for

Applications in Plasmonic Catalysis and Electrocatalysis

São Paulo

Deposit date at SPG

December 17th 2018

UNIVERSIDADE DE SÃO PAULO

INSTITUTO DE QUÍMICA

Programa de Pós-graduação em Química

VITOR RENATO RIBEIRO SILVEIRA

Nanocristais Ramificados de Ouro e Ouro-paládio para

Aplicações em Catálise e Eletrocatálise Plasmônica

Versão da dissertação defendida

São Paulo

Data de depósito na SPG

17/12/2018

VITOR RENATO RIBEIRO SILVEIRA

Gold and Gold-Palladium Branched Nanocrystals for Applications in Plasmonic Catalysis and Electrocatalysis

Dissertation Presented in the Chemistry Institute at the University of São Paulo in order to obtain the master's degree in Science.

Advisor: Pedro Henrique Cury Camargo

The original version of the dissertation

São Paulo

2019

Autorizo a reprodução e divulgação total ou parcial deste trabalho, por qualquer meio

convencional ou eletronico, para fins de estudo e pesquisa, desde que citada a fonte.

To my parents Elisa e Renato, who have always supported and loved me.

To my beautiful Camila, the love of my life, who has always been there for me.

ACKNOWLEDGMENTS

"To boldly go where no one has gone before.”

- Star Trek

ABSTRACT

Silveira, V.R.R. **Gold and Gold-Palladium Branched Nanocrystals for Applications in Plasmonic Catalysis and Electrocatalysis.** 2019. 75p. Master's Thesis - Graduate Program in Chemistry. Instituto de Química, Universidade de São Paulo, São Paulo.

The harvesting of solar light is one of the main challenges in science. The outstanding optical properties of plasmonic in the visible and near-infrared ranges due to the localized surface plasmon resonance (SPR) has emerged as a promising approach for the solar-to-chemical energy conversion. Specifically, it has been demonstrated that the SPR excitation in the visible range in silver (Ag) and gold (Au) nanoparticles can drive and accelerate chemical transformations. This field, coined plasmonic catalysis, enables one to merge catalytic and optical properties in the nanoscale and use visible or near-infrared light as a sustainable energy input to accelerate molecular transformations. In the first part of this thesis. we developed Au branched nanostructures to be employed as plasmonic catalysts. In this case, we aimed at investigating the effect of the sharp tips at their surface over their plasmonic catalytic performance, as it is established that tips can concentrate higher electric field enhancements relative to rounded surfaces as a result of the lightning rod effect, which, in turn, can translate into higher plasmonic catalytic performances. Here, the plasmonic-catalytic performances were tested using the SPR mediated oxidation of p-aminothiophenol and benzylamine as model transformations. While the Ag and Au nanoparticles support LSPR excitation in the visible and near-infrared ranges, their catalytic properties are limited in terms of versatility. Conversely, metals that are important in catalysis, such as palladium Pd, do not support SPR excitation in the visible or near-infrared range. In the second part of this thesis, we developed multimetallic nanoparticle morphologies, composed of both Au and Pd, that enabled us to marry catalytic and plasmonic component in order to address this challenge. We focused on plasmonic core-catalytic shell structures, in which the shell displayed a branched morphology. Parameters such as shell thickness could be controlled, and structure performance relationships were established towards the methanol electro-oxidation under plasmonic excitation.

Keywords: Nanocatalysts; Plasmonics; Photocatalysis; Electrocatalysis; Gold.

RESUMO

O aproveitamento da luz solar é um dos principais desafios da ciência. As excepcionais propriedades óticas plasmônicas nas regiões do visível e do infravermelho próximo, devido a ressonância plasmônica de superfície localizada (SPR), surgiram como uma abordagem promissora para conversão de energia solar em energia química. De maneira mais específica, vem sendo demonstrado que a excitação SPR na região do visível em nanopartículas de prata (Ag) e ouro (Au) podem conduzir e acelerar transformações químicas. Esse campo, chamado catálise plasmônica, permite a fusão de propriedades óticas e catalíticas na nanoescala e a utilização de luz visível ou infravermelha próxima como uma fonte de energia para acelerar transformações moleculares. Na primeira parte desta dissertação, nós desenvolvemos nanoestruturas de ouro ramificadas para serem empregadas em catálise plasmônica. Neste caso, nosso foco era investigar o efeito de pontas afiadas em sua superfície sobre seu desempenho catalítico plasmônico, visto que está bem estabelecido que pontas podem concentrar maiores intensificações de campo elétrico em relação a superfícies arredondadas como resultado do "efeito para-raios" o que, por sua vez, pode se traduzir em maiores desempenhos em catálise plasmônica. O desempenho da catálise plasmônica foi testado através da oxidação mediada por SPR do p-aminotiofenol e da benzilamina como reações modelo. Contudo, enquanto nanopartículas de prata e ouro apresentam excitação SPR nas regiões do visível e infravermelho próximo, suas propriedades catalíticas são limitadas em termos de versatilidade. Por outro lado, metais que são importantes em catálise, como o paládio, não apresentam excitação SPR no visível e infravermelho próximo. Por isso, na segunda parte desta dissertação, nós desenvolvemos nanopartículas multimetálicas, compostas de Au e Pd, que nos permitem unir os componentes catalíticos e plasmônicos com o objetivo de enfrentar este desafio. Nós focamos em estruturas do tipo core-shell, com núcleos plasmônicos e cascas catalíticas, na qual a casca apresenta morfologia ramificada. Parâmetros como a espessura da casca puderam ser controlados, e a relação estrutura-performance foi estabelecida através da eletro-oxidação do metanol sobre excitação plasmônica.

Palavras-chave: Nanocatalisadores, Plasmônica, Fotocatálise, Eletrocatálise, Ouro.

TABLE OF CONTENTS

1   Introduction

1.1   Nanomaterials: definitions, properties, and synthetic approaches

Nanomaterials have been used in cosmetics, electronics, drugs and a wide-ranging of technologies.[1-8] Nanomaterials can have different compositions (carbon[1,2], silicon[3,4], oxides[5,6], and metals[7,8]), but must present at least one of his dimensions between 1 – 100 nm.[9] The interest in nanomaterials has grown considerably since the early 1990s due to their unique properties and variety of applications. **Figure 1** shown this remarkable growth in terms of published papers with the keyword "nanomaterials".
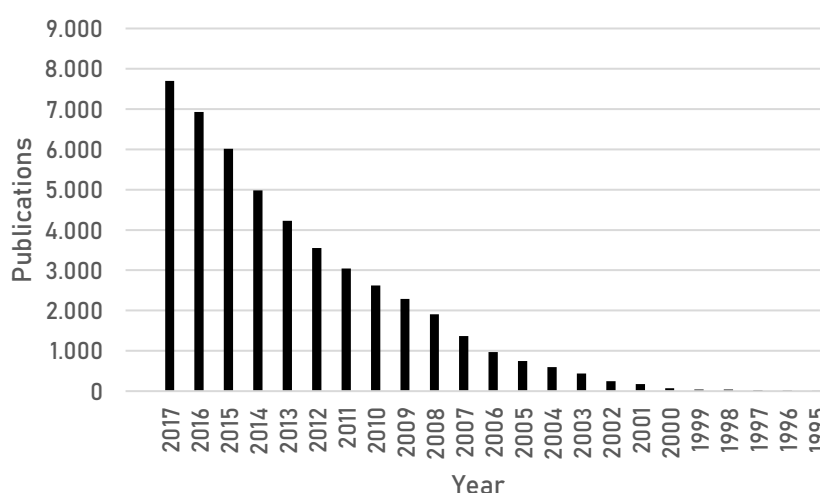
Figure 1. Publications per year since 1995 with the keyword "nanomaterials". (Web of Science)

The astonishing properties of nanomaterials are due to the large surface-to-volume ratios and quantum effects.[10] Nanoparticles, by definition, have large surface-to-volume ratios. For example, a hypothetical quasi-spherical nanocluster of 13 atoms has 12 of these atoms on the surface and only one inside. This corresponds to 92 % of atoms on the surface. If the quasi-spherical nanocluster has 8000 atoms (5 nm of diameter), the

proportion of surface atoms will be only 20 %.[10] **Table 1** shows the percentage of surface atoms as a function of the total atoms of the full shell "magic number" clusters (the more stable number of atoms for quasi-spherical hexagonal close-packed clusters). This better utilization of the atoms is important to applications that depend on the surface, such as catalysis.

Table 1. Percentage of surface atoms at clusters formed by shells with a different number of atoms. [11]

Number of shells	Number of total atoms	Number of surface atoms	Percentage of surface atoms (%)
1	13	12	92
2	55	42	76
3	147	92	63
4	309	162	52
5	561	252	45

In the nanoscale, the properties of a nanomaterial can be tuned by the manipulation of physical parameters such as size, shape, composition, morphology, and structure (solid or hollow interiors), which makes it possible the enhancement of properties for a target application. This manipulation is possible by the control of synthetic parameters during the synthesis.[7,12] The controlled synthesis of nanoparticles has been widely studied and is a powerful approach to tailoring reactivity and optical properties.[7,12]

Basically, there are two types of approaches to synthesize nanostructures: the top-down and the bottom-up methods.[13] In the first, large particles are fragmented until reach smaller sizes to form nanoparticles. In the second, growth occurs atom-by-atom until nanoparticles are formed. These approaches are shown in **Figure 2A**. In this work, the

bottom-up methods were chosen to produce the metallic nanostructures. We focused on the colloidal synthesis, due to their simplicity, versatility, low cost, scalability, and the potential for the use of green conditions. [7]

The colloidal synthesis can be divided into three major steps: nucleation, the evolution from nuclei to seeds, and evolution from seeds to nanocrystals.[7] These steps are represented in **Figure 2B**. In the first step, a metallic precursor is reduced to form the first atoms in solution (nuclei), which will be continuously formed. When their concentration reaches a critical point in the supersaturation regime, nucleation takes place.[12] These nuclei can fluctuate in shape as structural fluctuations to minimize surface energy can take place. As they grow, these structural fluctuations become more energetically costly, and they are locked into a specific morphology, representing the formation of the seeds (second step). With the seed formed, they can grow by atomic addition at their surface or by the aggregation of seeds to form the final nanocrystals.[7] It is important to emphasize that these steps of reduction and growth still being widely explored to understand the formation of nanostructures formation. This is a simple picture to approach the nanoparticle formation mechanism in colloidal synthesis.
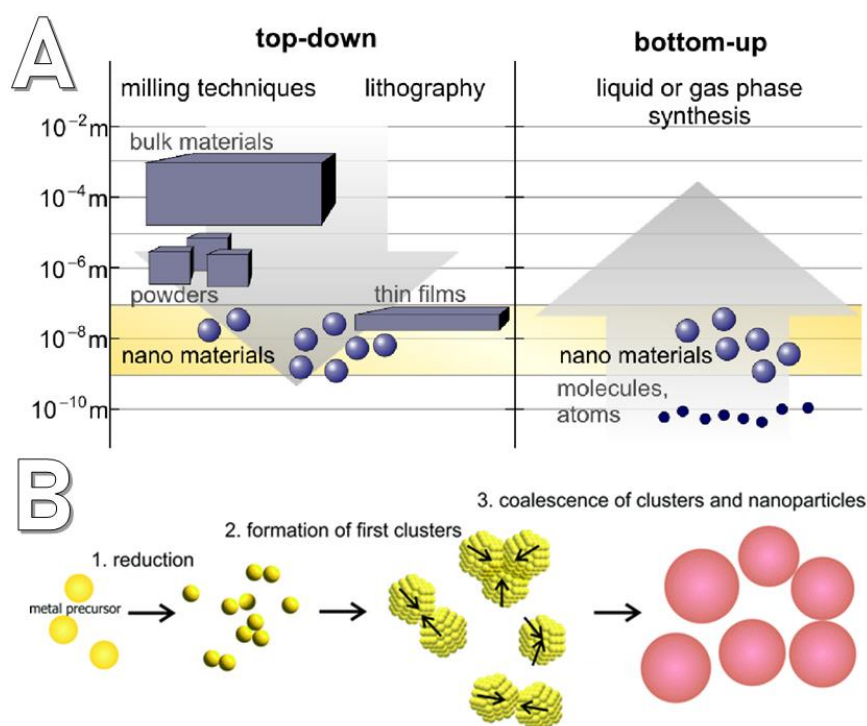
Figure 2. Schematic illustration of (A) the synthetic approaches top-down and bottom-up[14] and (B) the mechanism of metallic nanoparticle formation in colloidal synthesis.[15]

1.2 Metallic nanomaterials for catalysis and electrocatalysis

The catalytic activity in metallic nanomaterials is strongly dependent on the surface area. Thus, nanoparticles presented as an excellent option to the application in catalysis due to the elevated surface/volume ratio. Besides that, the control over nanoparticle shape and consequently the exposed facets on the surface, as shown in **Figure 3A**, can strongly influence catalytic properties. Many works have been demonstrating the correlation with the catalytic activity and selectivity with the crystallographic surface of nanostructures. This behavior is due to the different atomic packing and electronic state of the nanomaterial's surfaces. [16,17]

The {111}, {100}, and {110} are the most common surface facets to face-centered-cubic (*fcc*) unit cell. They differ by the occupation of the topmost layer by atoms which

following the order: {111} > {100} > {110}. Another important difference is the coordination number of the atoms on the surface. This can be noticed in **Figure 3B**, which shows that the atoms in {111} facet have 6 neighbors, the {100} has 4, and the {110} has 2. Because that, the surface energy for these facets follow the sequence {110} > {100} > {111}. As the {111} facet is the most stable (due to the higher coordination number) its reactivity is lower in comparison to {100} and {110}.[7,16,17] These factors act in catalytic processes influencing the adsorption, dissociation, coupling and the interact of intermediated adsorbates.
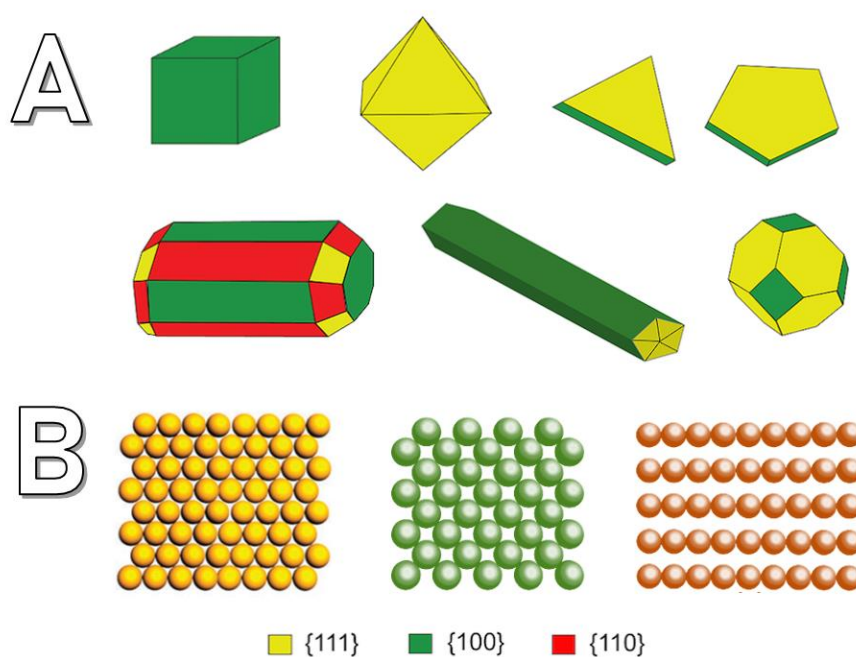
Figure 3. (A) Different shapes of nanoparticles. (B) The most common surface facets of FCC system: {111} (yellow), {100} (green), and {110} (red).[8,17]

Another important factor to the catalytic processes is the d-band center. The adsorption energies of molecules are strongly dependent on the electronic structure of the surface.[16] When an adsorbate and a metal surface interact, they can interact via d-σ

and d-σ* orbitals, for example (**Figure 4**). If the metal surface atom has a high d-band center in relation to the Fermi level, a decrease in the filling of (d-σ)* state occur, which make the metal-adsorbate bonding less destabilizing. In other words, the binding becomes stronger. On the other hand, when the atom has a low d-band center, an increase in the filling of (d-σ)* state occur, which make the metal-adsorbate bonding weak. The coordination number of atoms on the topmost layer influence the d-band center and therefore, the adsorption energy. Because that, different surface facets are expected to exhibit a differences in their d-band center, which affect the catalytic processes. [16,18,19]
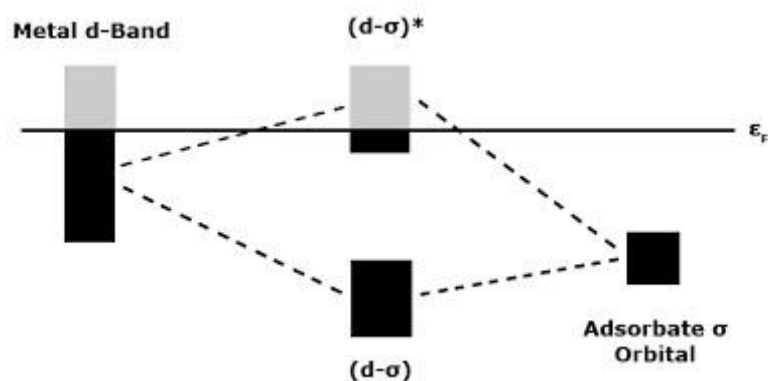
Figure 4. Diagram of the formation of bonding with a metal surface and an adsorbate.[19]

The controlled synthesis of nanomaterials is important to obtain control of these parameters which is the key to obtain enhanced catalytic activity and selectivity. In addition to the control over shape, another way to tune these properties is to manipulate composition to form multimetallic nanostructures and structure to form hollow nanomaterials. For example, in alloyed nanostructures, the metals are homogeneously mixed as a solid solution. On the contrary, in the core-shell and core-frame multimetallic nanostructures, the metals are segregated in distinct phases. Core-shell nanostructures

present a metallic core which is completely covered by a shell of another metal. In core-frame nanostructures, the core is partially covered by other metal.[16] Finally, hollow multimetallic nanoparticles (nanoshells, nanotubes, nanorattles, among others) present hollow interiors and increased surface areas relative to their solid counterparts. [20]

In this thesis, we are concerned in manipulating shape and composition (multimetallic nanomaterials). In the case over the control over shape, we are interested in developing nanomaterials with branched morphology, i.e., present tips at their surface. These systems enable increase surface-to-volume ratio relative to their rounded counterparts as well as tips that may display more reactive surfaces (exposure of higher index durface facets) and may enable one to concentrate increase electric-field enhancements as a result of surface plasmon resonance (SPR) excitation.[21–24] Regarding multimetallic nanomaterials, we are particularly interested in developing core-shell morphologies in this thesis. Core-shell nanostructures enables us to combine the individual properties of each metal in order to achieve a cooperative effect. Moreover, multimetallic nanostructures enables the synergism between the components. The synergetic interactions that are important to catalytic processes are often assigned to electronic and geometric effects. The first is caused by the modification of the electronic structure of the metals, affecting the charge transfer between the metals. This is a short-range effect and is only effective at most three atomic layers.[25] The geometric effects can be caused by the surface strain in which the atomic arrangement of the surface can be compressed or expanded due to the difference of the lattice parameter of the core and shell. This effect alters the d-band center due to the decreased (expanded) or increased (compressed) of the overlap of the d orbitals of the metallic atoms. [18,25]

It is noteworthy that, in addition to their widespread use in nanocatalysis, metallic nanoparticles have also been widely explored in electrocatalysis, especially in the context of fuel cells for clean energy generation/conversion.[26] In this sense, the electrooxidation of alcohols have been studied because they are possible substitutes for hydrogen in fuel cells.[27] In electrocatalysis, platinum and palladium are the most commonly used metals, but multi-metallic nanomaterials with noble and non-noble metals are also explored in order to improve activity, selectivity, and decrease the catalyst price.[16,28] Besides that, all previously discussed catalyst properties that influence the catalysis are also valid for electrocatalysis and their design is the key to obtain desired electrocatalytic activities.

1.3 Surface plasmon resonance (SPR)

Some metals display remarkable optical properties that can be put towards a variety of applications such sensing[29], energy generation[30], and catalysis[31]. In particular, it has been established that the electrons in metallic nanoparticles can oscillate from the equilibrium condition in response to an oscillating electric field component from an incoming electromagnetic wave (light).[32] This oscillation produces an electric dipole on the surface. The frequency of this oscillation is compatible with the wavelength of the light.[33] If the wavelength of the light match with the wavelength of natural oscillation of electrons, a constructive interaction (resonance) will occur. This phenomenon is called localized surface plasmon resonance (SPR). **Figure 5** shows a schematic illustration of the SPR effect. The term "localized" is used because the phenomenon also occurs in bulk materials but in these materials the oscillated is propagated on the "infinitely" metal surface. On the contrary, in nanoparticles, the effect is localized on a limited surface.

30,32,33
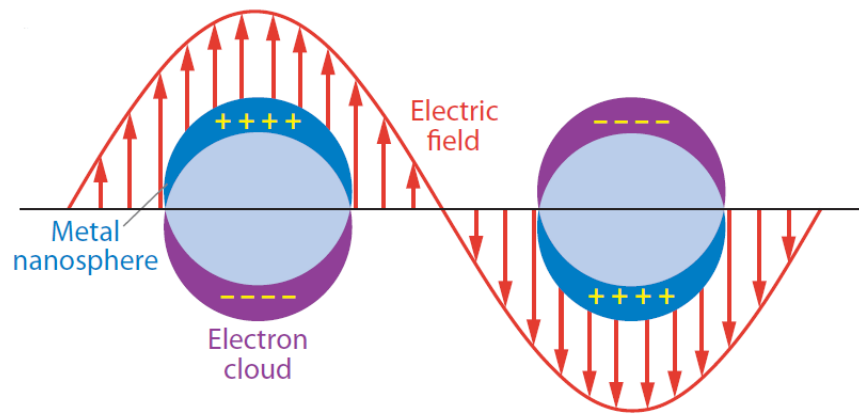
Figure 5. Schematic illustration of the localized surface plasmon resonance.[34]

The SPR frequency is dependent on size, shape, structure, composition, and dielectric constant of the environment.[35] This occurs due to the difference in surface polarization caused when the nanoparticle is illuminated by the light. The shape and size control of nanoparticle have been widely explored in order to tailor de optical properties of metallic nanoparticles and obtain an optimal activity for different applications.[33,36] **Figure 6** shows the difference between the optical properties of spherical and cubic silver nanoparticles. [36]
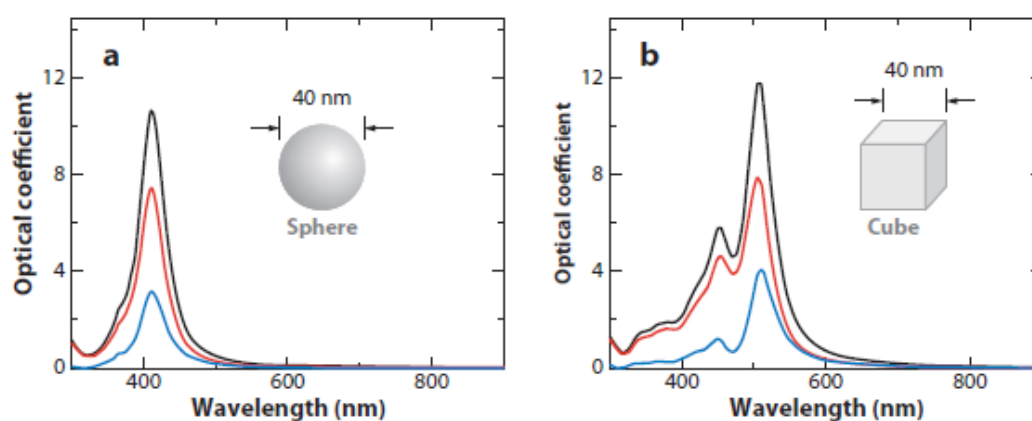
Figure 6. DDA-calculated extinction (black line), absorption (red line) and scattering (blue line) for (A) spherical and (B) cubic silver nanoparticles. [36]

1.3.1 *SPR-mediated catalysis (or Plasmonic catalysis)*

The SPR effect can be useful to drive, accelerate, and control chemical reactions on the surface of metallic nanoparticles.[33] In this sense, three physical effects can be highlighted: localized heating, optical near-field enhancement, and transfer of charge-carriers at the metal-molecule interface. [32]

The localized heating (**Figure 7A**) is generated as a result of SPR due to the resistance which the constituent metal offers when electrons oscillate through them, what is known by Joule effect. This heat, caused by dissipation of energy, can promote and accelerate chemical reactions. The heat generation is mostly explored in bio-related applications, such as photothermal therapy. [32] In the second effect (**Figure 7B**), electric fields are generated close to the nanoparticle's surface when the wavelength of light is adequate to generate de LSPR effect. This can enhance the absorption cross section in these regions, which can be expected to enhance photochemical reactions. This effect can be intensified by approaching two or more plasmonic nanoparticles, creating regions of high enhancement of electric field called hot spots. However, the probability of find a substrate exactly between two or more plasmonic nanoparticles is very small. In contrary, the probability of find the substrate on the surface of the nanoparticles is considerable. Therefore, another way to increase the hot spots is produce nanoparticles with a large number of tips or sharp edges (where the electric field enhancement is larger). [32,37]

The SPR excitation also leads to the formation of charge-carriers, such as hot electrons and holes. These, in turn, can be injected in an adsorbate acceptor orbital (**Figure 7C**) to activate these species and accelerate chemical transformations.[38] For example, many studies have been demonstrating the improvement of oxidative processes by the formation of O_2^- due to the SPR excitation.[31,39] Moreover, the hot electrons can

even promote the dissociation of H_2 on gold nanoparticles surface at room temperature, which was considered an impossible task without light irradiation.[40] Therefore, by the control of the optical properties of plasmonic nanoparticles, it is possible, at least in principle, to selectively inject electrons in specific orbitals improving the selectivity of catalytic processes.[32,33]
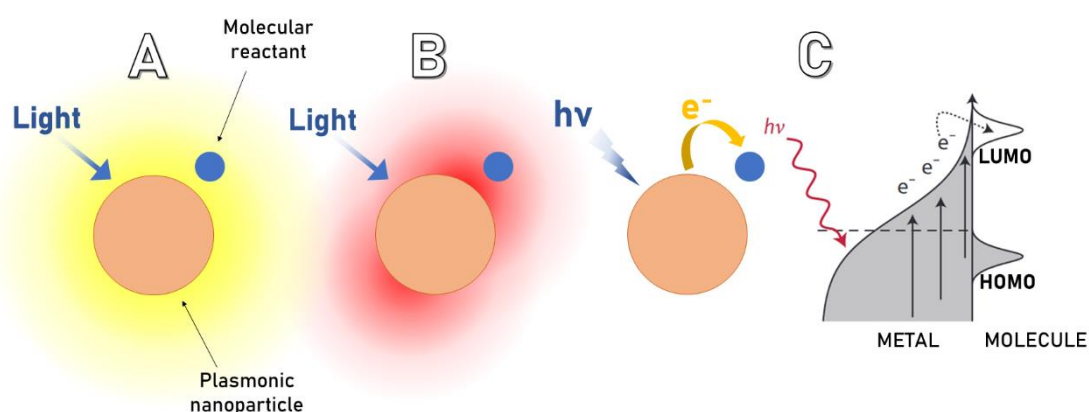
Figure 7. The SPR excitation in plasmonic nanoparticles can lead to: (A) localized heating, (B) electric field enhancement close to the nanoparticle's surface, and (C) photo-induced transfer of SPR-excited charge carriers to an adjacent molecule.[32,33]

These effects can occur simultaneously and separate the individual contribution of each effect is challenging. Because of this, the comprehension of the mechanisms of SPR-mediated reactions is an undergoing effort, which makes the plasmonic catalysis an exciting and promising area.

2   Objectives

The main objective of this work is to design the surface morphology and composition in of nanostructures comprising plasmonic and catalytic metals in order to obtain enhanced properities in terms of catalysis and electrocatalysis under visible light (plasmonic) excitation. More precisely, we chose to focus in the development of branched nanomaterials with the idea of achieving increased surface areas and higher electric-field enhancements as a result of SPR excitation to allow for a more efficient use of the surface and optical properties to improve the SPR-mediated catalytic processes.

Our first goal was to develop a facile and environmentally friendly synthetic approach to obtain highly branched Au nanostructures. Next, in our second goal, we wanted to probe the SPR-mediated activity of these nanostructures by employing the oxidation of p-aminothiophenol (PATP) to p,p'-dimercaptoazobenzene (DMAB) as a model transformation. Our third goal comprised to immobilize the nanostructures over a solid support (SiO$_2$) to generate supported plasmonic catalysts for liquid phase transformations. In this case, we employed the SPR-mediated oxidation of benzylamine to N-benzylidenebenzylamine as a proof of concept liquid phase reaction. In our fourth goal, we turned out attention to bimetallic plasmonic-catalytic nanomaterials having core-shell morphologies. We focused on a plasmonic-core Au and catalytic-shell Pd design in order to marry plasmonic and catalytic components. The goal was to use the plamonic metal to harvest light to enhance transformation at the surface of the catalytic metal, that do not support LSPR excitation in the visible range. In our fifth goal, we focused on Au-Pd core-shell nanostructures with different shell thickness to enable the establishment of structure-performance relationships in terms of performance. In our final goal, these nanomaterials, after being supported on Vulcan carbon, would be applied as model

systems in the plasmon-mediated photoelectrooxidation of alcohols. Overall, we aimed to obtain new insights over the factors that influence performance in plasmonic enhanced phenomena and enable the design of nanostructures with desired features and performances.

3 Materials and methods

3.1 Reagents

Table 2. List of used reagents.

Reagent	Formula	Purity (%)	Supplier
Chloroauric acid	$HAuCl_4 \cdot 3H_2O$	99.9	Sigma-Aldrich
Potassium Tetrachloropalladate	K_2PdCl_4	99.9	Sigma-Aldrich
Sodium Citrate	$Na_3C_6H_5O_7 \cdot 3H_2O$	99.0	Sigma-Aldrich
Polyvinylpyrrolidone (M_w=55,000 g mol^{-1})	$(C_6H_9NO)_n$	-	Sigma-Aldrich
Hydroquinone	C_6H_4-1,4-$(OH)_2$	99.5	Sigma-Aldrich
Ascorbic acid	$C_6H_8O_6$	99.0	Sigma-Aldrich
Sodium Hydroxide	$NaOH$	98.0	Sigma-Aldrich
Acetonitrile	CH_3CN	99.9	Sigma-Aldrich
Benzylamine	$C_6H_5CH_2NH_2$	99.0	Sigma-Aldrich
4-Aminothiophenol	$H_2NC_6H_4SH$	97.0	Sigma-Aldrich
Tris(hydroxymethyl)aminomethane	$NH_2C(CH_2OH)_3$	99.0	Sigma-Aldrich
Dodecane	$CH_3(CH_2)_{10}CH_3$	99.0	Sigma-Aldrich
Ethanol	CH_3CH_2OH	99.5	Synth
Isopropyl Alcohol	$(CH_3)_2CHOH$	99.7	Sigma-Aldrich
Silicon Oxide	SiO_2	-	-
Vulcan carbon	C	-	Cabot

3.2 Synthesis and plasmon-enhanced catalytic activity of branched gold nanoparticles

3.2.1 Synthesis of citrate-stabilized gold nanoparticles (Au seeds)

In a typical procedure, 0.5 mL of 25,4 mM $HAuCl_4$ aqueous solution (1 wt. %) was added to a 49.5 mL of a boiling sodium citrate aqueous solution (0.01 wt. %) under vigorous stirring. After 10 minutes of reflux, a red suspension of spherical gold nanoparticles were formed. [41]

3.2.2 Seed-mediated synthesis of gold nanourchins

In an ambient condition, 10 mL of 0.1 wt. % PVP55, 0.4 mL of Au seed's suspension and 0.085 mL of $HAuCl_4$ were added in a 25 mL round-bottom flask, and the mixture was kept under constant stirring. After 3 minutes 1 mL of 30 mM hydroquinone and 0.022 mL of 1 wt. % sodium citrate aqueous solution were simultaneously added to the reaction mixture which was maintained under stirring for 30 minutes. The influence of Au seed's quantity was explored changing the volume of suspension from 0.4 to 1 mL.

3.2.3 One-step synthesis of gold nanodendrites

The synthesis of gold nanodendrites is similar to the protocol used for gold nanourchins, differing only by the absence of Au seeds and volume of sodium citrate. In a 25 mL round-bottom flask was added 10 mL of 0.1 wt. % PVP55 and 0.085 mL of 25 mM $HAuCl_4$. After 3 minutes 1 mL of 30 mM hydroquinone and 0.300 mL of 1 wt. % sodium citrate aqueous solution were simultaneously added to the reaction mixture which was

maintained under stirring for 30 minutes. The influence of sodium citrate in the synthesis of gold nanodendrites was investigated changing the volume to 0, 0.100, 0.200, and 0.400 mL and the pH of the final suspension was measured in each case with a pH meter. The pH of sodium citrate 1 % was also measured and a sodium hydroxide aqueous solution with the same pH was prepared. The synthesis of nanodendrites was performed using 0.300 mL of sodium hydroxide instead of sodium citrate.

3.2.4 Synthesis of PVP-stabilized gold nanospheres (Au nanospheres)

In a typical synthesis, 6 mL of an aqueous solution containing 35 mg of PVP and 60 mg of ascorbic acid was prepared. This mixture was heated to 90 °C for 10 min with magnetic stirring. Then, 1 mL of 3 mM $AuCl_4^-{}_{(aq)}$ was added dropwise with magnetic stirring and the reaction was allowed to proceed for 3 h. The obtained Au NPs were washed several times with 1.5 mL of water by successive cycles of centrifugation and removal of the supernatant and re-suspended in water for further use.

3.2.5 Synthesis of Au/SiO₂ materials

The gold nanourchins, nanodendrites, and nanospheres were impregnated on commercial SiO_2 by the incipient wetness impregnation method.[42] For this procedure, the suspension of each nanostructure was batched synthesized (an appropriated amount to obtain 300 mg 2 wt.% Au/SiO_2) and concentrated in 5 mL of ethanol. The commercial SiO_2 was placed in a Petri dish and the concentrated suspension was added dropwise while being stirred by a metal spatula until all the ethanol evaporated. The Au in SiO_2 loading was determined with ICP-OES (Spectro Arcos).

3.2.6   SPR-mediated oxidation of benzylamine

The experiments were conducted using 20 mg of 2 wt.% Au/SiO$_2$, 5 mL of acetonitrile, 0.022 mL of benzylamine, and 0.022 mL of dodecane (internal standard) was added to a Fischer-Porter glass reactor which was purged and filled with 3 bar of O$_2$. The reactor was sonicated to suspend the catalyst in the mixture. For the reactions under visible light, the system was set 10 cm away from a 300 W halogen tungsten lamp (OSRAM) and was kept under stirring for 48 h. In this distance, the temperature reached 50 ºC due to thermal radiation. This temperature was used for the reactions in the dark which was performed in a bath. For the reuse tests the nanocatalysts was washed 5 times (1 time with ethanol followed by 4 times with acetonitrile) between the reuse cycles. The catalysis was performed in triplicate and the products and catalytic activity was determined using gas chromatography.

3.2.7   LSPR-mediated oxidation of PATP to DMAB

The Au nanodendrites, Au nanourchins, and Au nanospheres were suspended in 25 μL of H$_2$O. 25 μL of the resulting suspension was drop-cast onto a 1 × 1 cm Si(001) surface and dried in air. The sample was then immediately used for the Raman measurements. For SERS measurements, 40 μL of a 1.0 mM ethanolic solution of p-aminothiophenol was drop-cast on the corresponding Raman substrates, followed by drying under ambient conditions. All samples were used immediately for SERS measurements after preparation. Raman and SERS spectra were acquired on a Renishaw Raman System 3000 equipped with a CCD detector and coupled to a microscope. The laser beam was focused on the sample by using a 50x lens. The experiments were performed

under ambient conditions in a back-scattering geometry. The samples were irradiated with a (He-Ne) 633 nm line with controlled laser power outputs. All Raman spectra were acquired in a single scan with 10 s accumulation time. All spectra were normalized with respect to the Raman band at 1081 cm^{-1} for the ease of comparison.

3.3   Synthesis and plasmon-enhanced electrocatalytic activity of branched Au@Pd core-shell nanostructures

3.3.1   Seeded growth synthesis of tris-stabilized gold nanoparticles (Au Nps)

The 33 nm tris-stabilized gold nanoparticles were grown from the previously synthesized Au seed's (synthesized as described in 3.2.1). In an ambient condition, 27 mL of deionized water, 1 mL of 0.1 M Tris aqueous solution, 10 mL of Au seed's suspension and 1 mL of 25 mM HAuCl$_4$ aqueous solution was added to a 50 mL round-bottom flask under stirring. After 1 min 1 mL of H$_2$O$_2$ (30 wt. %) was added into the mixture solution. The reaction was maintained under stirring for 30 minutes.[41]

3.3.2   Synthesis of Pd nanobushes (Pd Nps)

In a 100 mL round-bottom flask was added 45.5 mL of 0.1 wt. % PVP55 and 2,5 mL of 30 mM hydroquinone aqueous solution which were heated to 60 ºC under stirring. After 3 minutes 2.5 mL of 24 mM K$_2$PdCl$_4$ was increased to the mixture. This mixture was kept under heating and stirring for another 30 minutes.

3.3.3 Synthesis of Au@Pd core-shell nanodendrites

In a typical procedure, 3 mL of tris-stabilized gold nanoparticles (Au Nps) suspension was centrifuged at 7000 rpm, the supernatant was removed, and the nanoparticles were resuspended in 10 mL of 0,1 wt. % PVP55. This suspension was heated to 90 ºC under stirring and 0.2 mL of 24 mM K_2PdCl_4 aqueous solution was added. After 1 minute 0.5 mL of 100 mM hydroquinone was rapidly added to the reaction mixture. The reaction was removed from heat after 1 hour. The same process was repeated for 0.3 and 0.4 mL of 24 mM K_2PdCl_4 adapting proportionally the volume of hydroquinone to obtain different shell thickness of Pd.

3.3.4 Synthesis of Au@Pd/C, Au/C, and Pd/C materials

To immobilize Au@Pd core-shell nanodendrites on Vulcan carbon the wet impregnation method was chosen. Each synthesis of Au@Pd was repeated 15 times to obtain the appropriate volume to synthesize 50 mg of Au@Pd 10 wt. % metal on carbon. This volume of suspension was concentrated and resuspended in 30 mL of ethanol. Then this new suspension was heated to 78 ºC under stirring and 50 mg of Vulcan carbon was added to the mixture which was maintained under reflux for 1 hour. After this, the suspension was heated to 100 ºC to evaporate ethanol. The same methodology was employed for Pd/C and Au/C, where 50 mL of suspension was used in both cases. The loading of Au and Pd in Vulcan carbon was determined with ICP-OES (Spectro Arcos).

3.3.5   Electrochemical characterization

The electrochemical measurements were performed at 25°C (± 2°C) using a Autolab PGSTAT 302N potentiostat/galvanostat with a conventional three-electrodes cell. A Pine® glassy carbon (GC) electrode (area = 0.1963 cm²) was used as working electrode and a platinum wire as counter electrode. A reversible hydrogen electrode (RHE) was used as reference electrode coupled to cell by a luggin capillary. Before each measurement, the working electrode was polished with alumina suspension with 0.3 µm and 0.05 µm and cleaned using sulfuric acid (0.5 mol L^{-1}).

The catalyst ink composed of catalyst powder (1mg), distilled H_2O (1 mL) and isopropilic alcohol (20 µL) was sonicated by 30 minutes using a 40 kHz ultronique (eco-sonic®) ultrasonic bath. 5 µL of catalyst ink was pippeted onto glassy carbon electrode and dried at N_2 flux in room temperature. Five microliters of Nafion solution (5%, Sigma Aldrich®) in distilled water 1:100 (v/v) ratio was added onto electrode after ink film dry.

The electrochemical measurements were performed in N_2 saturated 1 mol L^{-1} KOH (≥ 85%, Sigma -Aldrich) electrolyte for three times, and the average of collected data were presented. For the electrocatalyst surface clean, cyclic voltammetries (CV) were recorded from 0.5 to 1.2 V (vs RHE) at a scan rate of 100 (20 cycles), 50 mV s^{-1} (10 cycles) and 20 mV s^{-1} (3 cycles), then the third cycle obtained at 20 mV s^{-1} was used to characterize the surface. The activity toward methanol and CO oxidation reactions was measured by cyclic voltammetries from 0.05 to 1.2 V (vs RHE) at a scan rate of 20 mV s^{-1}. For MOR the CV was performed in 1 mol L^{-1} KOH + 1 mol L^{-1} CH_3OH solution while for CO oxidation, the electrolyte was saturated with CO holding the working electrode at 0.1 V (vs RHE) during 5 minutes. After that, N_2 was purged for 25 minutes and the stripping curves was collected in CO-free solution under the same electrochemical conditions of methanol oxidation.

Both methanol and CO oxidation reactions were carried out under absence and presence the green light source (532 nm – 200 mW) illumination. The photocurrent experiments were performed at 0.7 V (vs RHE) during 300 seconds in the same conditions of the MOR.

4 Results and discussion

4.1 Synthesis and plasmon-enhanced catalytic activity of branched Au nanomaterials

Hydroquinone has been demonstrated as an interesting reductant for the synthesis of Au nanospheres[43–45] and branched nanostructures[46,47] at room temperature. Regarding optical properties, branched nanostructures may display high electric fields at the tips and at junctions between branches.[21] In order to explore the optical properties of branched nanoparticles and how these structures can enhance catalytic properties via the SPR excitation, we focused on the synthesis of Au nanodendrites (in the absence of seeds) and nanourchins (in the presence of seeds). In this work, a facile one-step synthesis of Au nanodendrites at room temperature was developed. This synthesis is based on a rapid reduction of $AuCl_4^-$ by the reductant mixture of hydroquinone and sodium citrate.[46] In our case, the utilization of sodium citrate proved essential for size, shape, and monodispersity. **Figure 8A-E** shows TEM images of the Au nanodendrites as a function of the amount of sodium citrate employed during the synthesis.
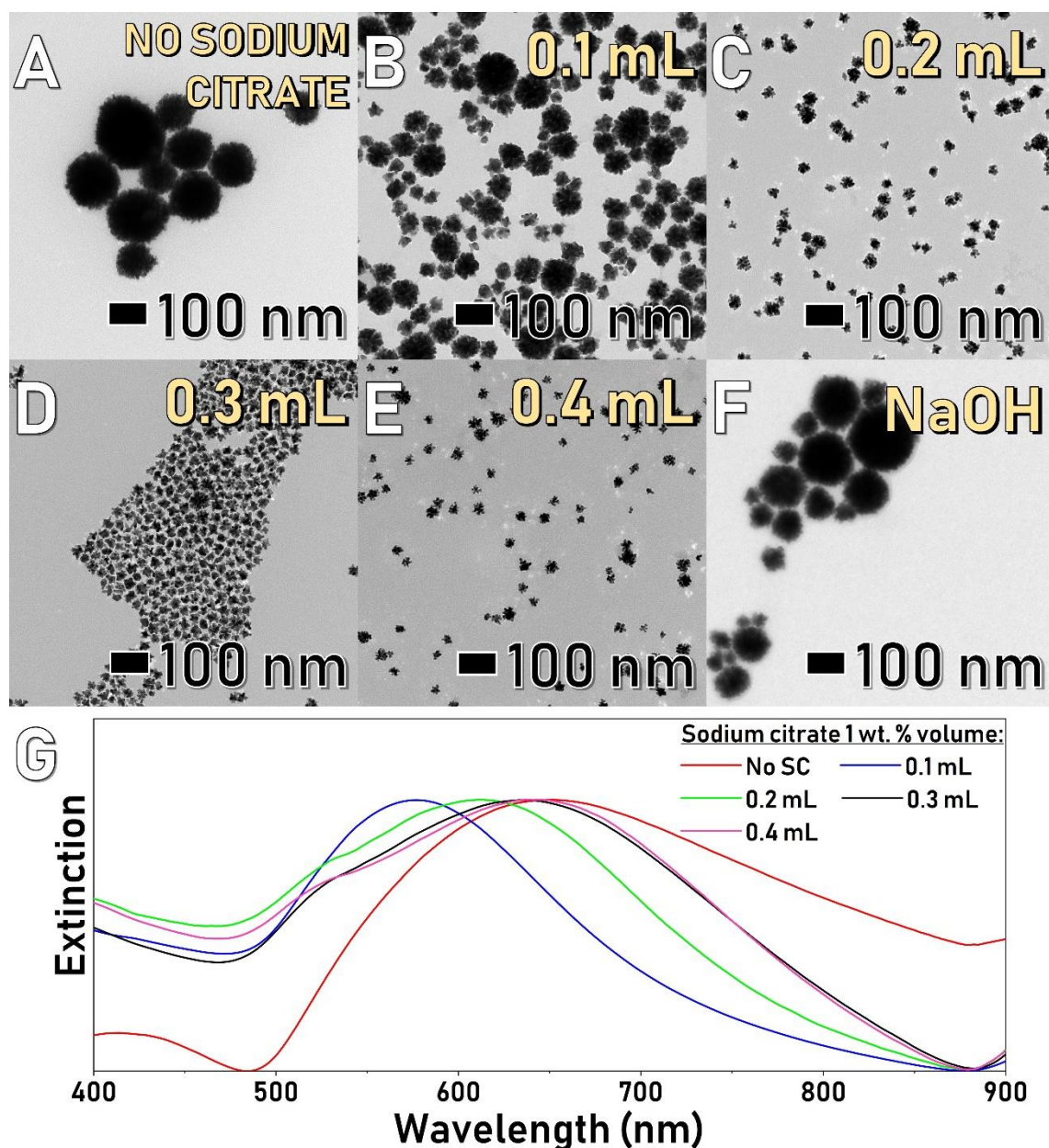
Figure 8. TEM images of Au nanodendrites synthesized with (A) no sodium citrate (B) 0.100 (C) 0.200 (D) 0.300 (E) 0.400 mL of sodium citrate 1 wt. %, and (F) 0.300 mL of sodium hydroxide aqueous solution with pH = 8. (G) UV-Vis extinction spectra of the suspension of nanodendrites synthesized with different volumes of sodium citrate 1 wt. %.

In absence of sodium citrate, we observed largely branched nanoparticles with approximately 100 - 150 nm of diameter. In the presence of sodium citrate, we observed

the formation of longer branches and a decrease in the size of the nanodendrites with the increase in volume of this reductant. We also observed in our experiments that 0.3 mL was the ideal volume of sodium citrate 1 wt.% to obtain an optimal size distribution of nanodendrites. **Table 3** shows the increase of the pH of the suspension after the reaction with the increase of the volume of sodium citrate. In fact, it is well known that this reductant has an important role as a pH controller in the formation of Au nanoparticles.[48]

Table 3. pH of the suspension of gold nanodendrites synthesized changing the volume of sodium citrate 1 wt. %

Sodium citrate 1 wt. % volume (mL)	pH
No sodium citrate	3.25
0.100	3.90
0.200	5.68
0.300	6.00
0.400	6.24

In order to check the function of sodium citrate as a pH controller, a sodium hydroxide solution with the same pH of sodium citrate 1 wt. % (pH = 8) was used instead of sodium citrate. Nanostructures similar to those formed without sodium citrate were obtained (**Figure 8F**). So, we noticed that sodium citrate does not work only as pH controller, but also contribute in the reduction and stabilization process during nucleation and growth stages to generate the Au nanodendrites.

In addition to the morphologies, the optical properties of these nanostructures were strongly dependent of sodium citrate volume as shown in the extinction spectra recorded from aqueous suspensions containing the nanostructures (**Figure 8G**). It can be observed that the SPR band are shifted to longer wavelengths with the increase of the

volume of this reductant. Due to these observations, the volume of sodium citrate 1 wt.%

chosen to synthesize the nanodendrites under optimized conditions was chosen as 0.3

mL. **Figure 9A-C** show TEM, STEM-HAADF, and HRTEM the images of the nanodendrites

obtained under these conditions. They were monodispersed, displayed well-defined and

uniform branches at their surface, and were obtained with controlled shapes. They were

32.4 ± 2.6 nm in diameter. The HRTEM of the branches (**Figure 9C**) shows a lattice spacing

of ~ 2.21 Å which indicates that the surface branches are made mainly by {111} facets.

Figure 9D shows {200} facets which are detected only in a small fraction in the

nanodendrites. Similar behavior has already been observed in other branched

nanoparticles. [49]

We also prepared Au nanourchins by seeded growth, in which a similar strategy

was employed as described for the nanodendrites, but in the presence of Au nanoparticles

as seeds for further Au deposition and growth (heterogeneous nucleation and growth).

Figure 9E shows the TEM images for the Au nanourchins. They were 60.1 ± 4.5 nm

indiameter and displayed controlled shapes and sizes. They were less branched than

nanodendrites as shown in the STEM-HAADF image (**Figure 9F**). In fact, branches appear

to also be larger. Besides, the {111} and {200} lattice spacings facets (**Figure 9G** and **H**)

appear to be more present in the branches in comparison to nanodendrites. **Figure 9I**

shows the extinction spectra for the nanodendrites, nanourchins, and nanospheres 18.4

± 2.2 nm in diameter that were prepared for comparison (benchmarking of optical

properties and SPR-mediated catalytic performances). A redshift in the SPR band as we

move from the spheres to the nanodendrites and nanourchins can be observed as a result

of the increase in size and presence of tips at their surface, which enables a larger charge

separation during plasmon oscillation.[36]
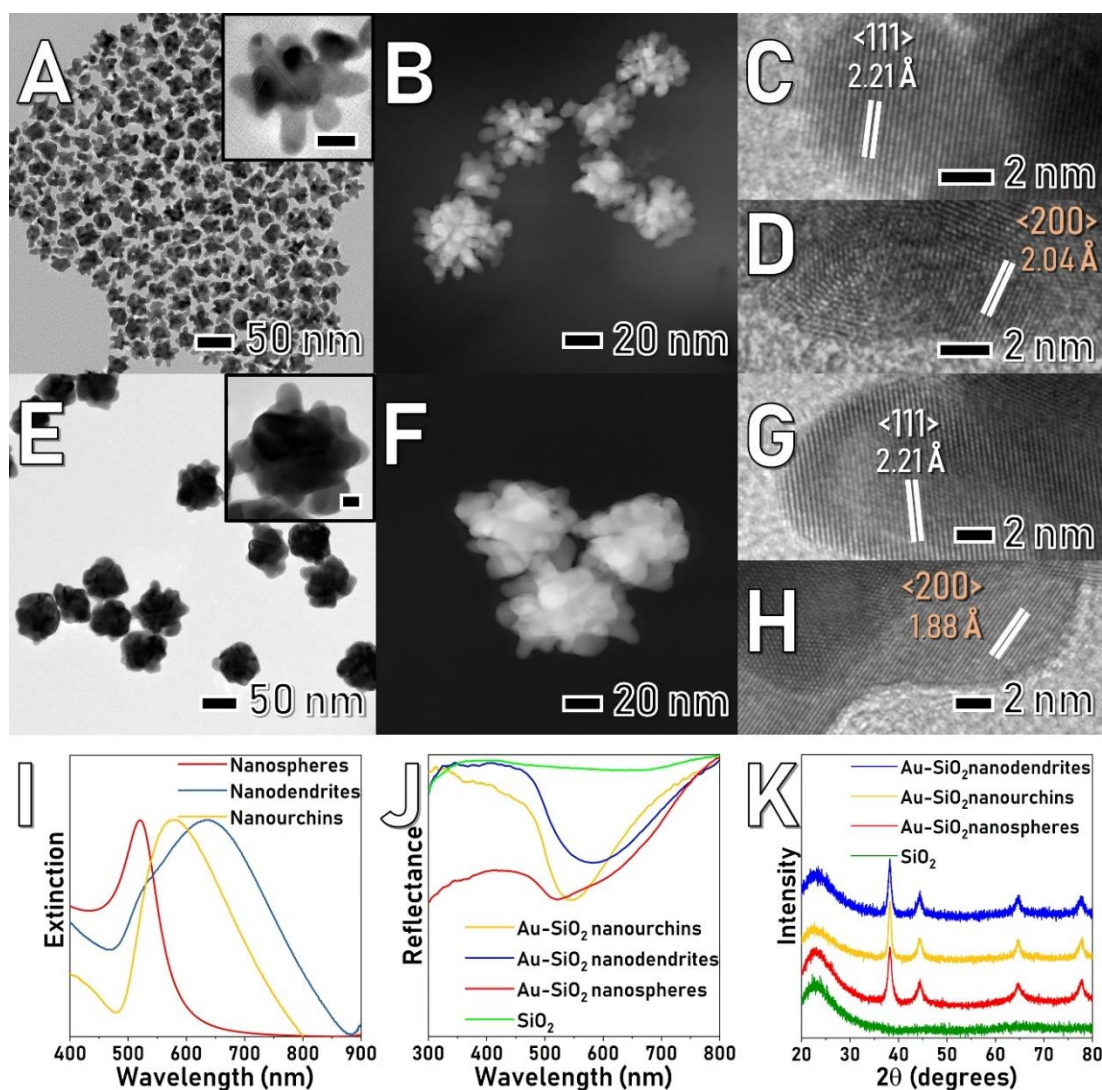
Figure 9. (A) TEM, (B) STEM-HAADF, and (C-D) HRTEM images of Au nanodendrites. (E) TEM, (F) HAADF, and (G-H) HRTEM of Aunanourchins. (I) UV-Vis extinction spectra of the suspension of nanospheres (red), nanodendrites (blue), and nanourchins (yellow) (J) Diffuse reflectance of SiO_2 (green), nanospheres (red), nanodendrites (blue) and nanourchins (yellow) immobilized on SiO_2 (K) XRD patterns of SiO_2 (green), nanospheres (red), nanodendrites (blue), and nanourchins (yellow) immobilized on SiO_2. The scale bars in the A and D insets correspond to 20 nm.

After their synthesis, the Au nanodendrites, nanourchins, and nanospheres were immobilized on SiO_2 to prepare the corresponding supported catalysts (denoted Au-SiO_2) supported catalysts. **Figure 9J** shows the diffuse reflectance for pure SiO_2 and the Au-SiO_2 nanostructures. It was observed a blue shift on the wavelengths in comparison to UV-VIS extinction spectra which was probably due to the changing on the refractive index of the surrounding dielectric media due to their deposition in SiO_2. The signal from the plasmonic component (Au) can be detected in all spectra for Au-SiO_2, and the same trend was detected relative to the extinction spectra. The XRD patterns for Au-SiO_2 are shown in **Figure 9K** which is according with the presence of *fcc* Au and amorphous SiO_2. The SEM images for the Au-SiO_2 materials (**Figure 10A-C**) shows that the Au nanostructures were immobilized on SiO_2 with uniform distribution over the support and no considerable agglomeration over large areas. The corresponding histograms of the size distribution of Au nanodendrites, Au nanourchins, Au nanospheres, and Au seeds employed in the synthesis of the nanourchins are shown in **Figure 11A-D**.
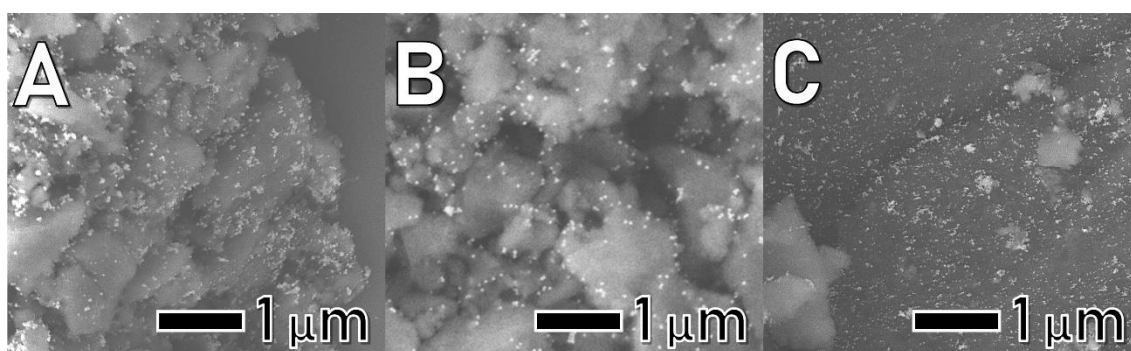
Figure 10. SEM images of Au nanodendrites (A), nanourchins (B), and nanopheres (C) supported on SiO_2.
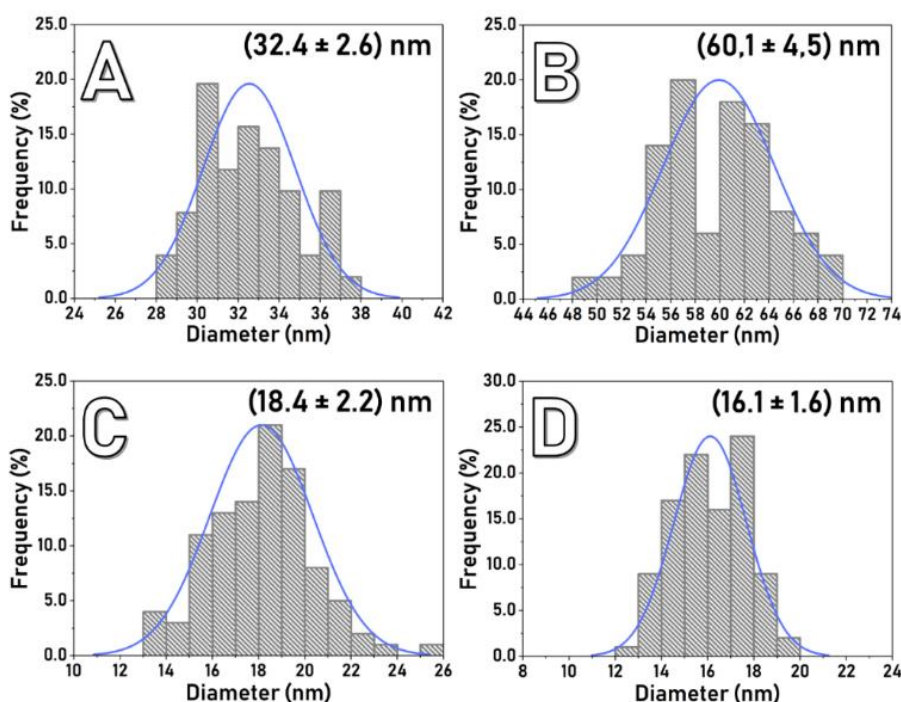
Figure 11. Histograms of size distribution for Au nanodendrites (A), nanourchins (B), nanoparticles (C), and seeds (D).

After the synthesis and characterization of the obtained Au nanodendrites, Au nanourchins, and Au nanospheres, we turned our attention to the investigation of the SPR-mediated catalytic activities as a function of their size and shape. We were particularly interested in probing the morphological dependence of the nanoparticles on the plasmonic catalytic activities. In fact, Au nanoparticles have recently been widely explored as an effective catalyst, especially for aerobic oxidative transformations.[50–52] The shape and morphology of these materials have also been investigated in order to obtain more efficient harvesting of light in photocatalysis applications.[53–55] However, branched gold nanoparticles have been poorly studied to date towards this application.

We started by probing the SPR-mediated oxidation of PATP functionalized at the Au surface to DMAB as a model transformation according to the following Equation (1).[56]

$$2AuS–Ph–NH_2 + {}^3O_2 + hv \rightarrow AuS–Ph-N=N–Ph-SAu + 2H_2O \quad (1)$$
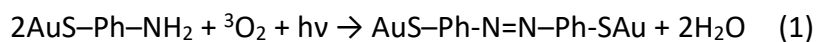
Here, it has been established the LSPR excitation in Au nanomaterials can lead to the formation of hot electrons, i.e., electrons that transiently occupy energy states above the Fermi level during plasmon oscillation.[33,57] These hot electrons can be transferred to an adsorbed molecule displaying suitable empty energy levels available, and this trigger charge-transfer transformations. In the context of LSPR-mediated PATP oxidation, the hot electrons produced from Au excited nanoparticles can be transferred to adsorbed O_2 molecules (from the air), which are activated to ${}^2O_2{}^-$ ions, which subsequently contribute to the PATP oxidation to DMAB at the metal surface. [58,59]

The laser-power-dependent spectra employing 632.8 nm as the excitation wavelength for nanodendrites, nanourchins and nanospheres that had been functionalized with PATP are shown in **Figure 12A-C**, respectively. The spectra contain two sets of bands: (i) the signals at 1081, 1142, 1390, 1433 and 1575 cm^{-1} that can be assigned to the Ag modes of DMAB; and (ii) the signals at 1081, 1489 and 1593 cm^{-1} that can be assigned to the A_1 modes of PATP. The PATP conversion can be monitored from the 1433:1081 cm^{-1} DMAB:(PATP + DMAB) intensity ratios which are depicted in **Figure 12D**.[42] **Figure 12D** show the DMAB:(PATP+DMAB) ratio for the Au nanostructures, indicating that the SPR-mediated catalytic activity increased in the order: nanospheres < nanourchins < nanodendrites. Nevertheless, the DMAB:(PATP+DMAB) intensity ratios became more intense as the laser power increased, in agreement with a SPR-mediated process.[60]
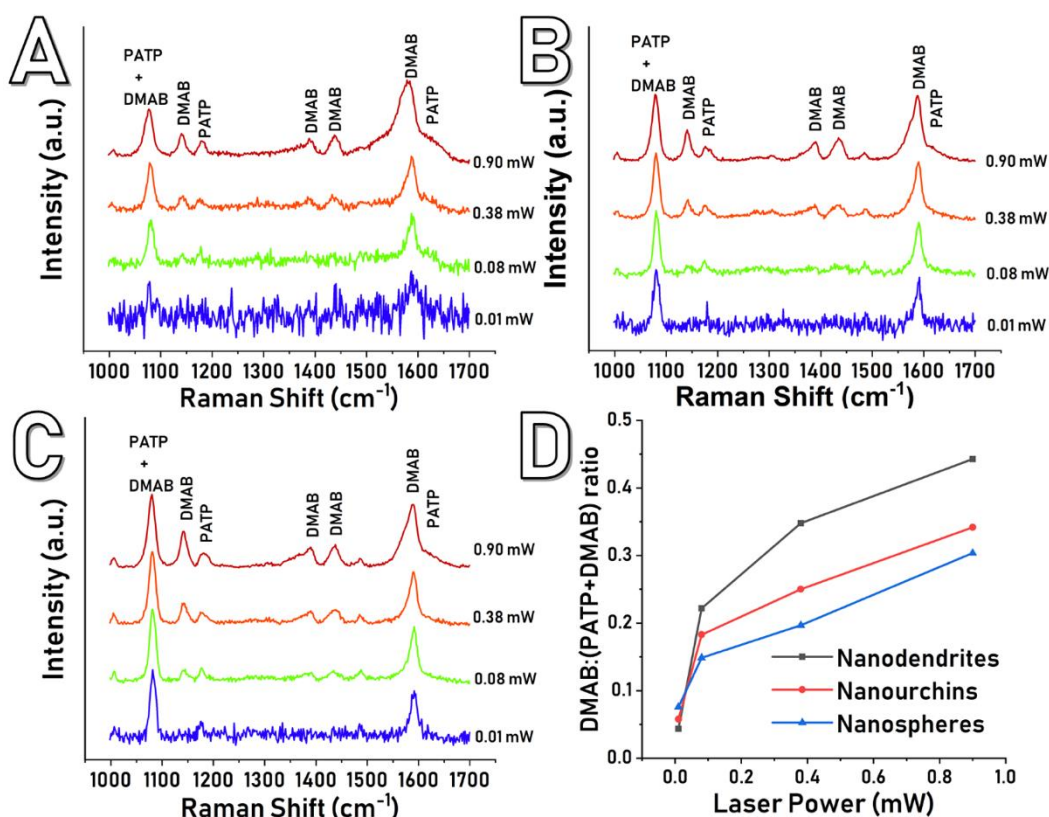
Figure 12. Laser-power-dependent SERS spectra for Au nanodendrites (A), nanourchins

(B), and nanospheres (C) that had been functionalized with PATP at 0.01, 0.08, 0.38 and

0.90 mW with an exposure time of 10 s. All spectra were recorded employing 632.8 nm

as the excitation wavelength and were normalized with respect to the band at 1081 cm^{-1}.

(D) Laser-power-dependent SPR-mediated oxidation of PATP, expressed as the

DMAB:(PATP+DMAB) ratio, for Au nandendrites, nanourchins, and nanospheres (black,

red and blue lines, respectively).

The observed variations in the catalytic activity of Au nanoparticles could be

explained on the basis of the matching between the SPR position and wavelength of the

incoming electromagnetic radiation employed as the excitation source (632.8 nm). In this

case, a close matching would lead to a higher LSPR excitation, leading to the generation

of a larger population of hot electrons that would participate in the LSPR-mediated

oxidation of PATP. Our experimental UV-visible spectra (**Figure 9I**) clearly shows that the LSPR have extinction maximum of 635, 580 and 520 for Au nanodendrites, nanourchins, and nanospheres, respectively. These observations indicate a stronger matching between SPR position and excitation wavelength, leading to stronger SPR excitation which would lead to higher E-field enhancements. These, in turn, may lead to the formation of a higher number of hot electrons that would be available for charge transfer and mediate the PATP oxidation. The superior catalytic activity of nanodendrites can also expected because of the presence of branches, that can concentrate more intense E-fields relative to the spheres and may enable the presence of electromagnetic hot spots between the branches. In fact, the presence of a larger number of branches that are more closely positioned to each other in the nanodendrites relative to the nanourchins can also contribute to its higher SPR-mediated PATP conversion.[61–63] Our results demonstrate that the optimization over the morphology of Au nanostructure play a very important role over the optimization of SPR-mediated activities.

These outstanding optical properties and the elevated surface area makes the nanodendrites and nanourchins possibly good choices to be used as plasmonic catalysts towards liquid phase transformations. In this context, we employed these nanostrucrures supported on SiO_2 (Au-SIO$_2$ materials) as plasmonic catalysts towards the aerobic liquid phase oxidation of benzylamine to N-benzylidenebenzylamine. The reaction was conducted for 48 h in a Fisher-Porter glass reactor filled with 3 bar of O_2 and using acetonitrile as solvent. The excitation source was a 300 w tungsten lamp positioned 10 cm away from the reactor. The temperature radiated measured from the lamp under this distance was 55 °C. The reactions in the dark were performed in the same conditions but

in the absence of the Xe lamp. The conversion (%) in dark and under light excitation are shown in **Figure 13**.
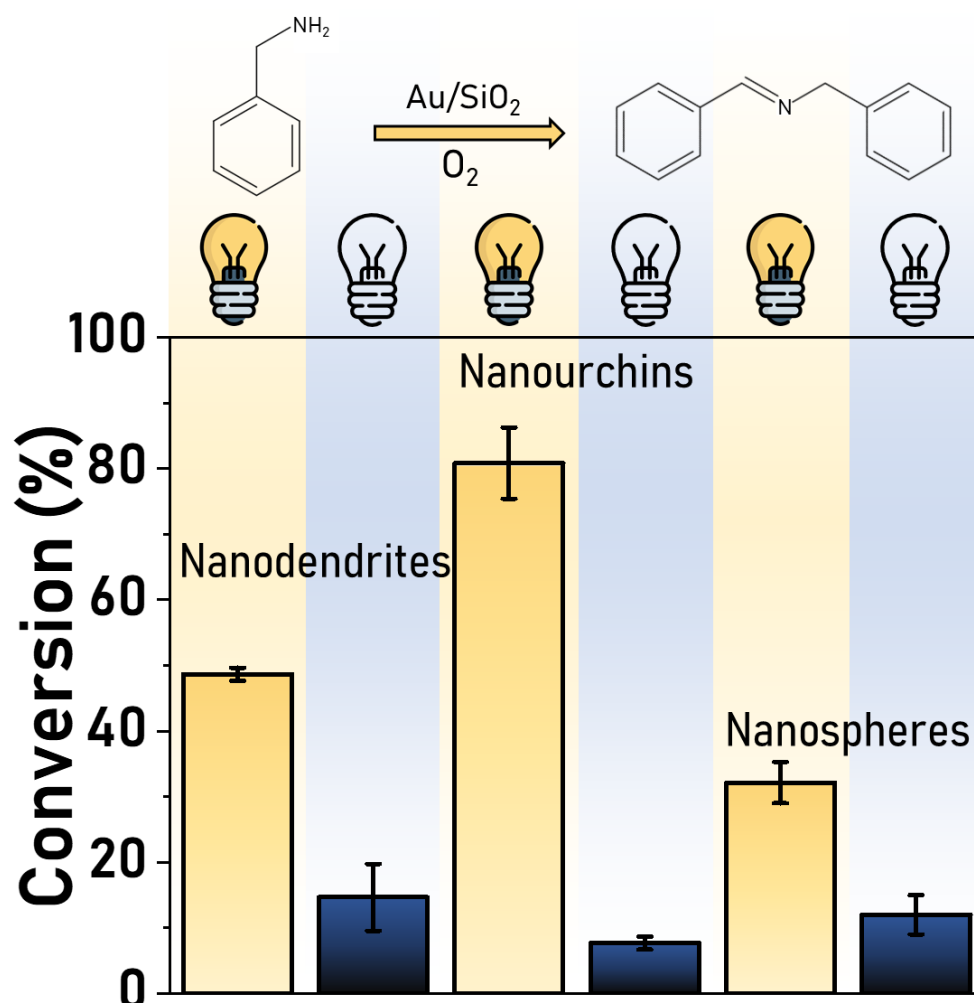
Figure 13. Oxidation of benzylamine to N-benzylidenebenzylamine in dark (blue bars) and under light excitation (yellow bars). The reaction was performed with a molar ratio Au:substrate of 1:133 (0.2 mmol of benzylamine and 0.0015 mmol of Au) in 5 mL of acetonitrile under 50 °C and 3 bar of O_2 for 48 h. No reaction was observed when no catalyst was used.

As expected, in dark, nanodendrites and nanospheres have better activities than nanourchins due to their smaller size (higher surface area). For all the materials, an increase in conversion % was observed under light irradiation due to the SPR excitation.

However, contrary to what was oberved for the PATP conversion, the nanourchins displayed a higher conversion % relative to the nanodendrites and nanospheres towards the benzylamine oxidation. Here, we would like to propose that these variations in conversion % may be due to the lower stability of the nanourchins under the reactions conditions. In fact, under the employed conditions (that required more energy relative to the SPR mediated PATP oxidation), we noticed that the branched nanostructures have undergone significant changes in their shape, as shown in **Figure 14**, becoming more ronded after 48h. It can be observed that the nanodendrites turned totally to spherical nanoparticles. These results highlight the importance of the study of stability of nanoparticles in the field of plasmonic catalysis. [64,65] Surprisingly, this issue remains overlooked in most studies in the area of plasmonic catalysis.
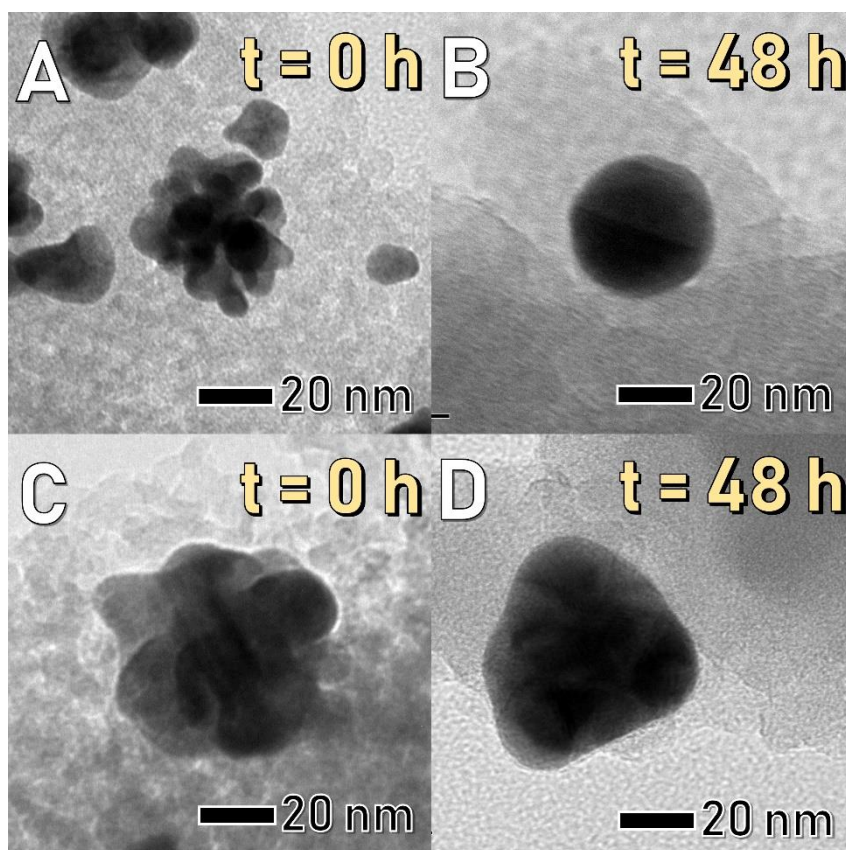

Figure 14. Supported nanodendrites (A and B) and nanourchins (C and D) before and after the benzylamine oxidation.

Therefore, the lower catalytic activity of nanodendrites relative to the nanourchins for the benzylamine oxidation in the liquid phase can be explained by their poor stability under the conditions of this catalysis. On the contrary to the reaction in the dark, the comparatively larger size of nanourchins is favorable for the reaction under illumination. The combination of shape stability (relativelly to nanodendrites and nanospheres) and branched nanostructure makes the nanourchin a better catalyst than nanodendrites and nanospheres to the plasmon-mediated oxidation of benzylamine in the liquid phase. However, the stability of both catalysts need to be addressed. For instance, by employng nanourchins in reuse tests towards benzylamine oxidation under visible ligh (**Figure 15**), the conversion % becomes significantly decreased during sucessive reaction cycles.
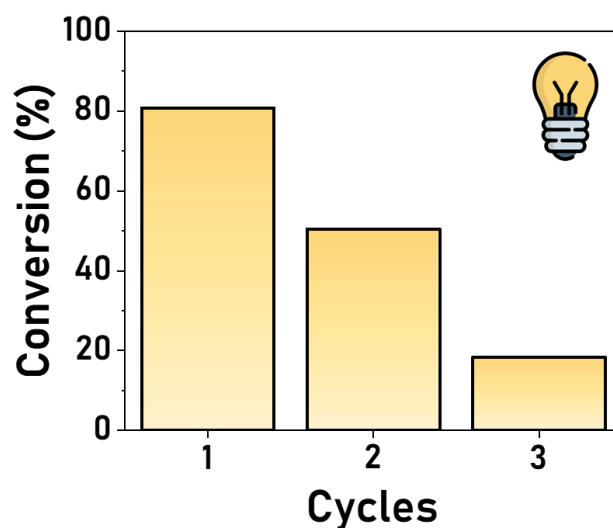

Figure 15. Catalytic stability tests employing Au nanourchins in benzylamine oxidation.

Finally, the suggested mechanism for plasmonic enhanced catalytic transformation described herein based on the charge transfer of SPR-excited hot electrons to O_2 molecules (generating O_2^- species) are summarized in **Figure 16**.
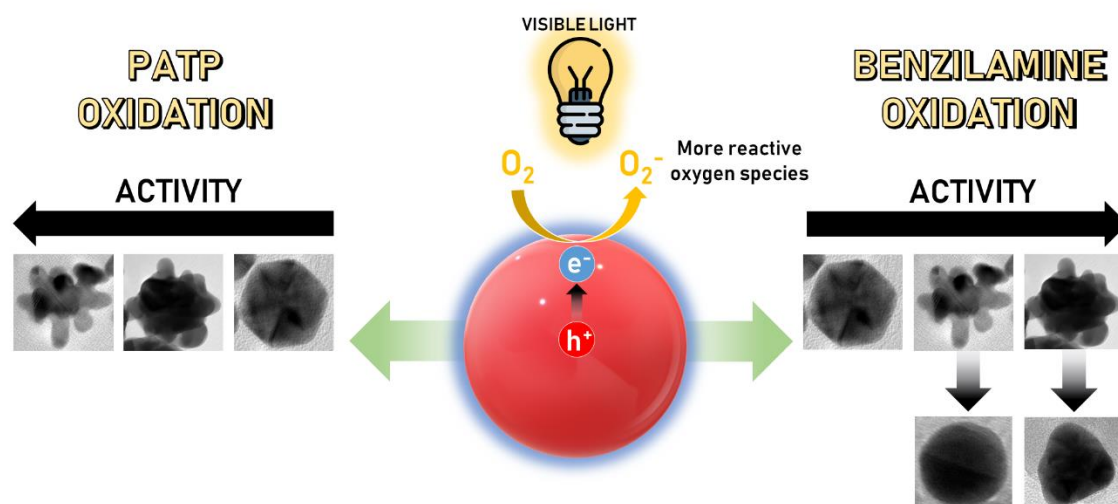
Figure 16. Schematic illustration of the plasmon-mediated formation of activated O_2 due to the charge transfer of SPR excited hot electrons to adsorbed O_2. This activated O_2 them participates and accelerates further oxidation processes.

4.2 Synthesis and plasmon-enhanced electrocatalytic activity of branched Au@Pd core-shell nanostructures

Au and Ag nanoparticles, due to their SPR excitation in the visible range, have been widely explored in the field of SPR-mediated catalysis. However, these metals are not highly catalytically active for a wide range of reactions as compared to more catalytic metals such as platinum (Pt) and palladium (Pd). In this context, the idea of marrying plasmonic and catalytic components multimetallic nanostructures (having both catalytic and plasmonic metals) has emerged as an elegant and efficient strategy.

Here, we are particularly interested in nanomaterials containing both Au and Pd, in which Au can be employed to harvest energy from light to potentially accelerate chemical transformation at the surface of the Pd (catalytic) metal. Specifically, we focused on Au@Pd core-shell nanoparticles. We decided to prepare a variety of Au@Pd core-shell systems in which we tuned the thickness of the Pd shell and employed these materials to

understand how plasmonic-catalytic activity depends on these physicochemical parameters (composition and shell thickness).

We started with the synthesis of Au@Pd by a seeded-mediated approach, in which Au nanoparticles 33 nm in diameter were employed as physical templates of Pd deposition at its surface by using hydroquinone as a reducing agent.[66] In this case, the thickness of the Pd-based shells could be controlled by varying the amount of Pd precursor employed during the synthesis. **Figure 17** shows a schematic illustration of our synthesis procedure.
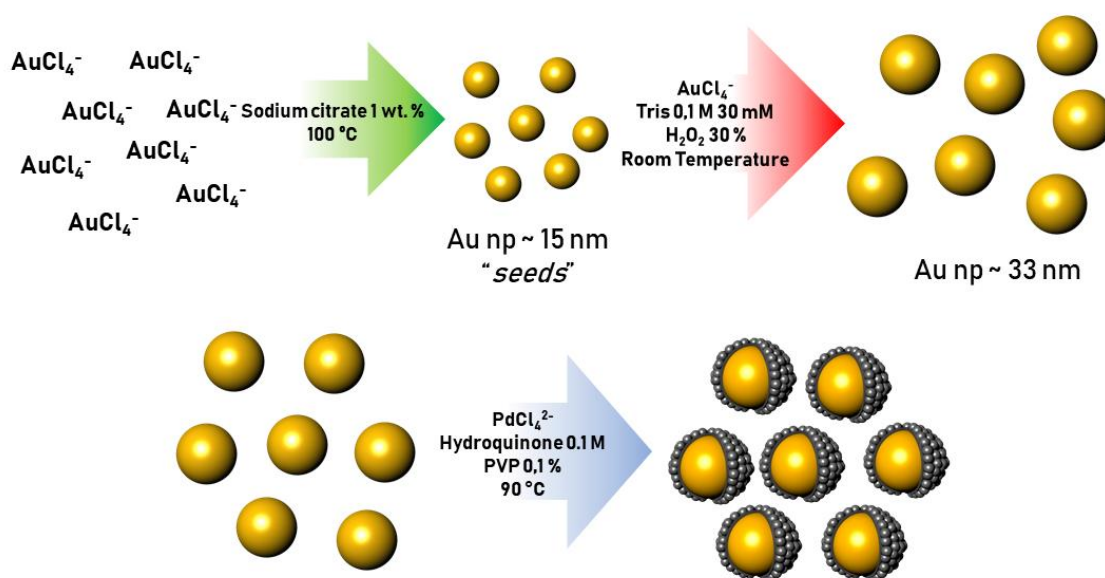
Figure 17. Schematic illustration of the synthetic approach to produce Au@Pd nanostructures.

The SEM (**Figures 18A-C**) and TEM (**Figure 18D-F**) images of Au@Pd nanostructures obtained by this approach employing different amounts of Pd precursor during the synthesis indicate that the Au@Pd nanoparticles are monodisperse, spherical, and have well-controlled shapes and sizes. The Pd shells have a dendritic-like morphology, probably related to the utilization of hydroquinone as a reducing agent. It has been established that

hydroquinone favor the formation of branches due to its preferential adsorption at {111} surface facets in Pd nanomaterials.[67] Moreover, it can be detected that our strategy effectively enabled the control over the Pd shell thickness, which corresponded to 9.0 nm (**Figure 18A** and **D**), 12.0 nm (**Figure 18B** and **E**), and 14.0 nm (**Figure 18C** and **F**). These core-shell Au@Pd nanomaterials were denoted Au@Pd-1, Au@Pd-2, and Au@Pd-3, respectively.
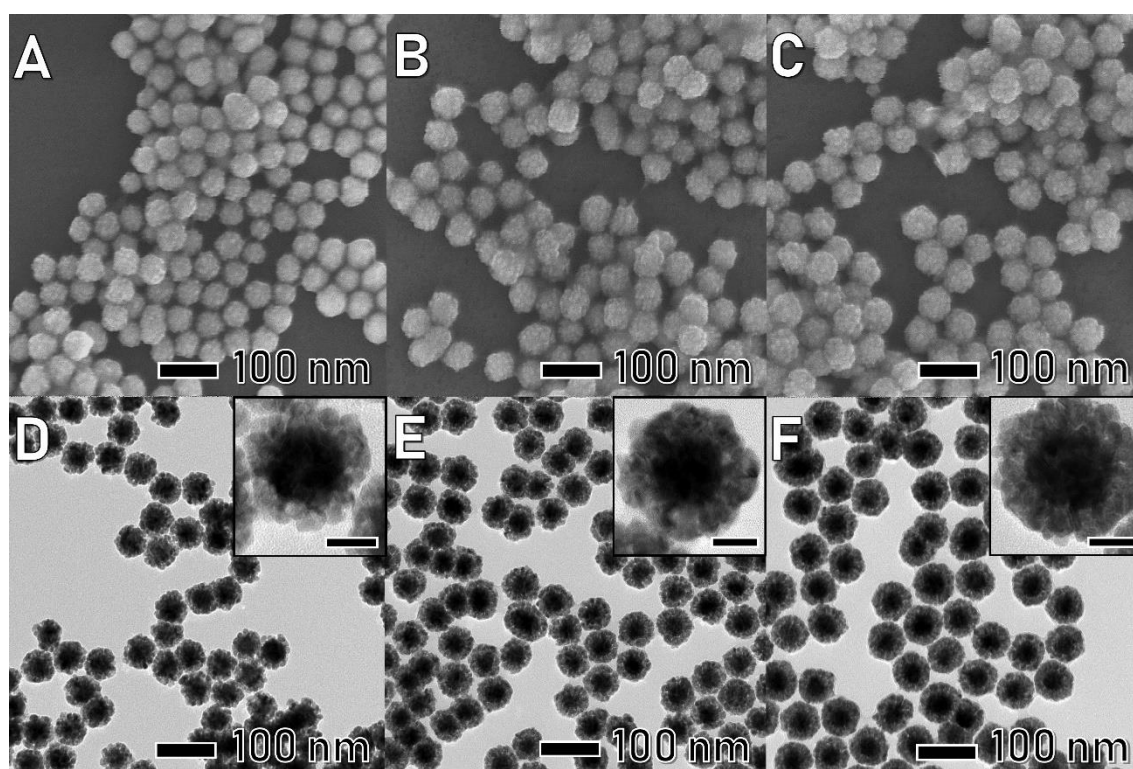
Figure 18. SEM and TEM images of Au@Pd core-shell nanodendrites with 9.0 (A and D, Au@Pd-1), 12.0 (B and E, Au@Pd-2), and 14.0 nm (C and F, Au@Pd-3) in shell thickness. The scale bars in the insets correspond to 20 nm.

The growth mechanism of this synthesis is based on the nucleation of clusters of Pd which is added on the surface of the core for the formation of a core-shell structure.[68,69] The presence of some of these clusters in the final suspension support this mechanism. They can separated by centrifugation as shown in **Figure 19**.[68]
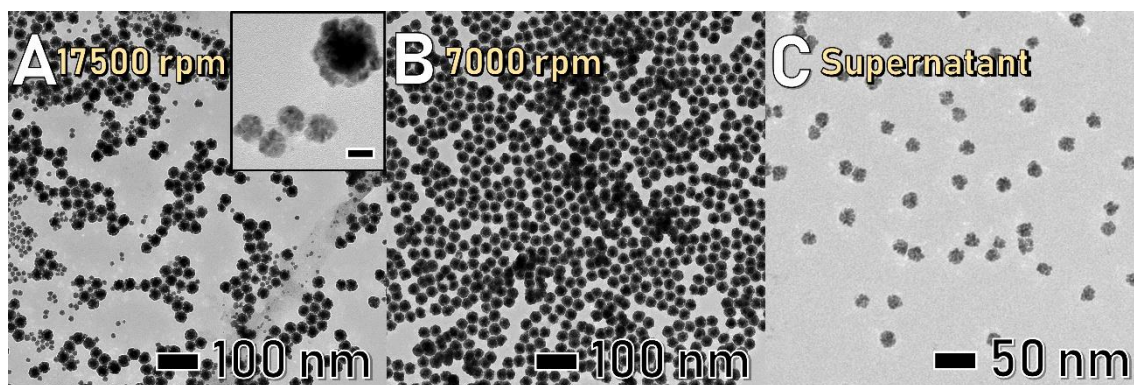
Figure 19. TEM images of Au@Pd core-shell nanodendrites (A) Centrifuged at 17500 rpm (B) Centrifuged at 7000 rpm (C) Supernatant removed from suspension centrifuged at 7000 rpm. The scale bar in the inset corresponds to 20 nm.

Figure 20A-E shows a STEM-HAADF (**Figure 20A**), STEM-EDX elemental maps for the distribution of Au (**Figure 20B**), Pd (**Figure 20C**) and the overlay maps (**Figure 20D**), and a HRTEM images (**Figure 20E**) for the Au@Pd-1 sample. The presence of a branched shell and the concentration of Au and Pd at the core and shell regions of the nanoparticles, respectively, can be clearly observed. Moreover, the 2.15 Å lattice spacings corresponding to the {111} planes of Pd *fcc* structure can be visualized in the HRTEM image.
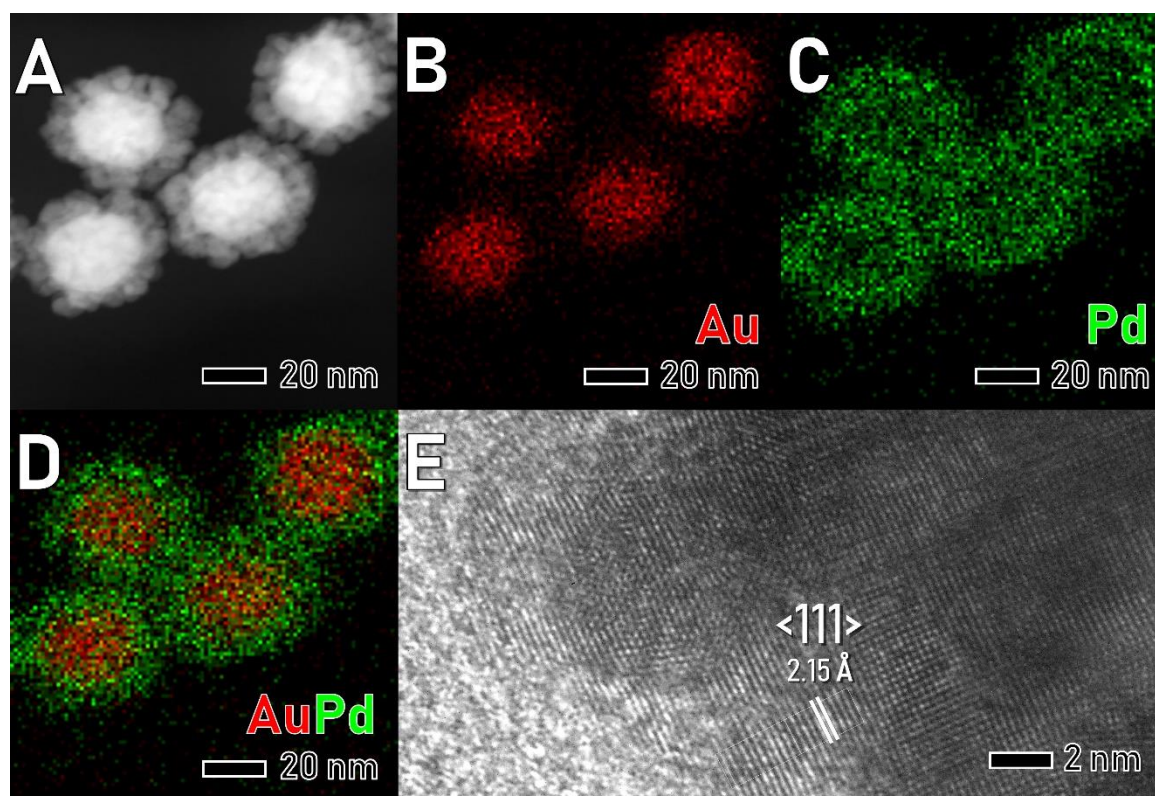
Figure 20. STEM-HAADF (A); STEM-EDX elemental maps for Au (B, red), Pd (C, green), and Au and Pd overlay (D); and HRTEM image for Au@Pd-1 core shell sample.

In order to benchmark the performances of the Au@Pd core-shell nanoparticles against their monometallic individual counterparts, we prepared Au nanoparticles 33 nm in diameter (as shown in **Figure 21A and C**) and the Pd nanoparticles 62 nm in diameter (as shown in **Figure 21B and D**). They were also uniform, monodisperse, and presented similar shapes relative to the Au@Pd core-shell material.
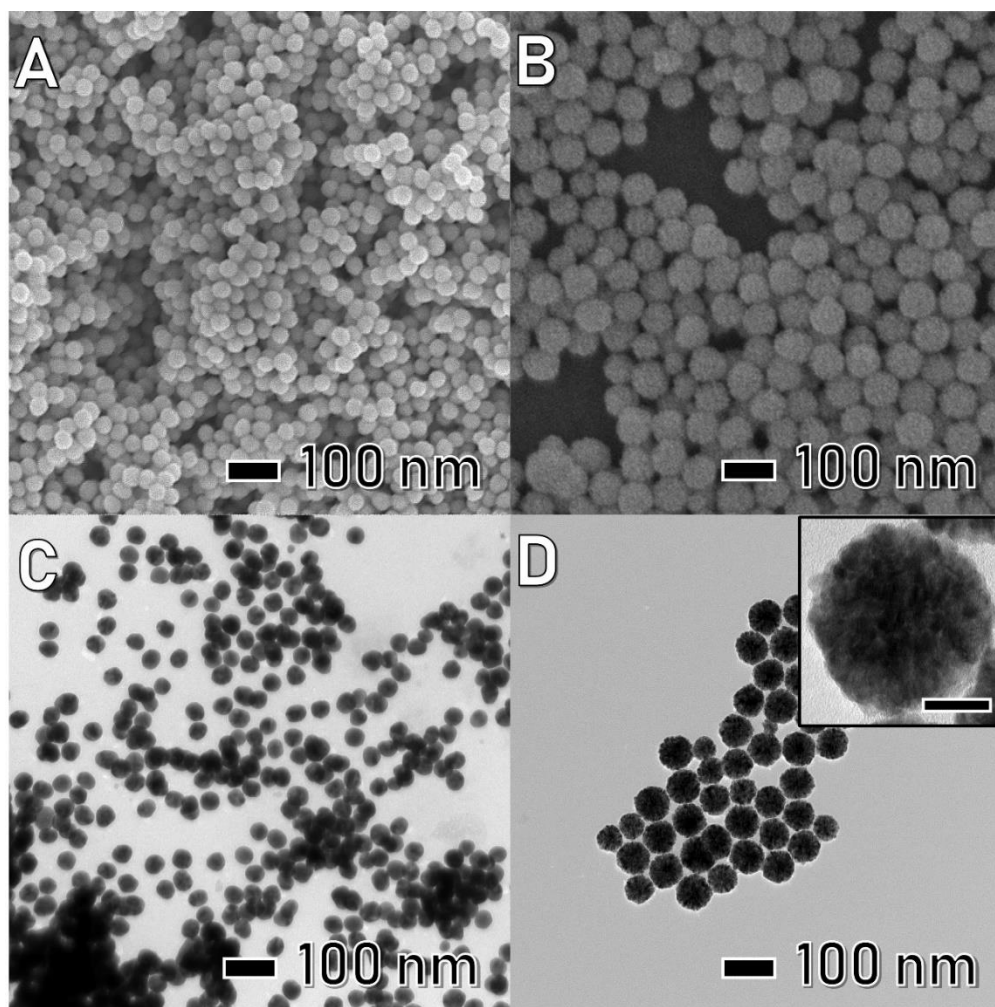
Figure 21. SEM and TEM images of monometallic Au (A and C) and Pd (B and D) nanostructures that were employed as standards to benchmark the performance of the Au@Pd nanomaterials.

The histograms of the size distribution for the Au@Pd-1, Au@Pd-2, Au@Pd-3, Au, and Pd nanoparticles are shown in **Figure 22A-E**, respectively.
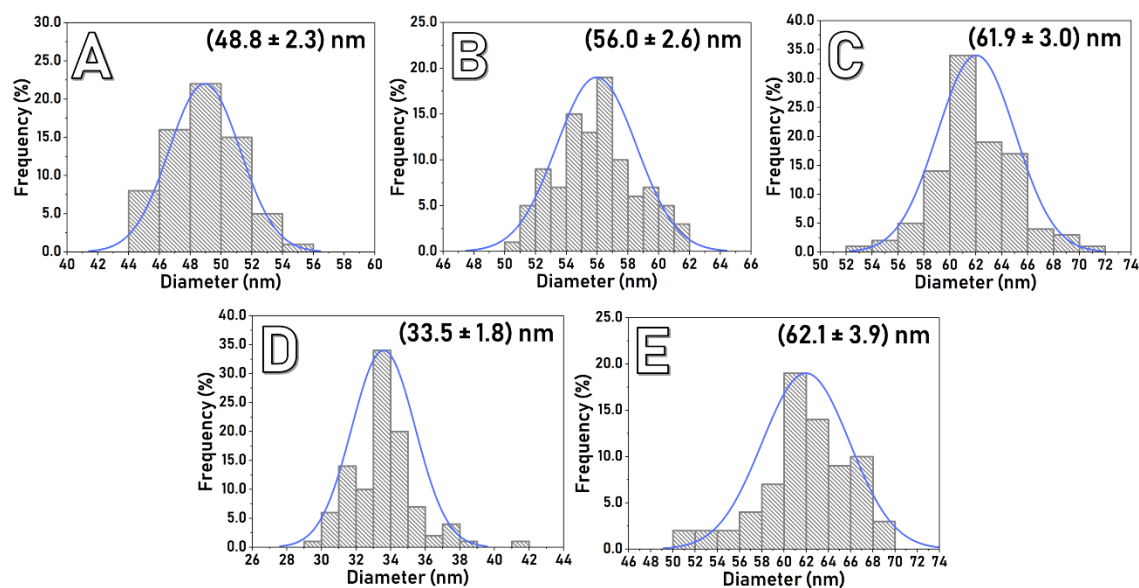
Figure 22. Histograms of size distribution for the Au@Pd-1 (A), Au@Pd-2 (B), Au@Pd-3 (C), Au nanospheres (D), and Pd nanoparticles (E).

The Au@Pd, Au, and Pd nanoparticles were then supported on Vulcan carbon to generate solid materials to be employed as electrocatalysts. The Vulcan carbon was chosen as support because of the high surface area, chemically inert and conductive characteristic. The SEM images (**Figure 23A-E**) shows the nanostructures supported in Vulcan carbon with a uniform dispersion without significant agglomeration over large areas.
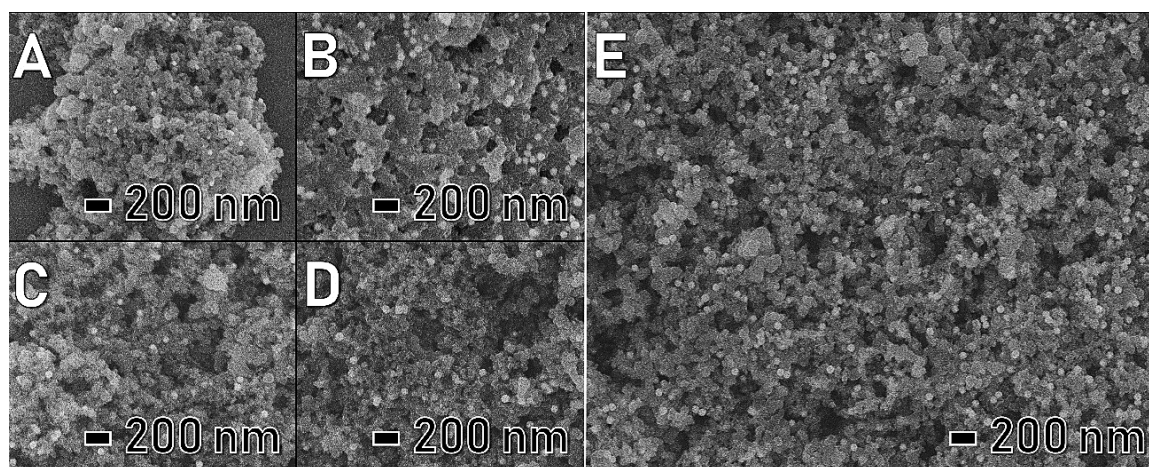
Figure 23. SEM images of Au (Au), Pd (B), Au@Pd-1 (C), Au@Pd-3 (D), and Au@Pd-2 (E) supported on Vulcan carbon.

Figure 24A shows the extinction spectra of Au, Pd, and Au@Pd with three different shell thickness. As expected, the palladium shell attenuates the SPR from the Au core with the increase of thickness. This leads to a blue shift on SPR extinction band.[70] The XRD patterns of the nanostructures supported on Vulcan carbon are shown in **Figure 24B** are in agreement with the presence of *fcc* Au and Pd (and amorphous carbon). However, a shift in the Au and Pd diffraction peaks in the core-shell diffractograms can be noted. This observation can be attributed as an evidence of small Pd size in the branches and the presence of geometric effects (lattice strain). For our case, the latter is more likely. Strain effects has been observed in many works as a factor that can change the surface energy and consequently the reactivity of nanomaterials. The XRD of strained nanostructures exhibit shifts in the peaks which is related to distortions in crystal lattice due to lattice mismatch between metal crystal structure of core and shell.[71,72] As we can observe in **Figure 24B**, the right-shift in Au peaks of Au@Pd/C nanostructures are very close to those of the Au/C which indicate that the Au core is not significantly strained (compressed). On the other hand, a great distortion (expansion) of Pd lattice is evidenced by Pd {220} peak which was highly left-shifted in comparison to Pd/C nanomaterial. Because of their unique surface properties, strained nanostructures (for example Au@Pd core-shell) has been used as a more efficient catalyst for electrocatalysis. [72–74]
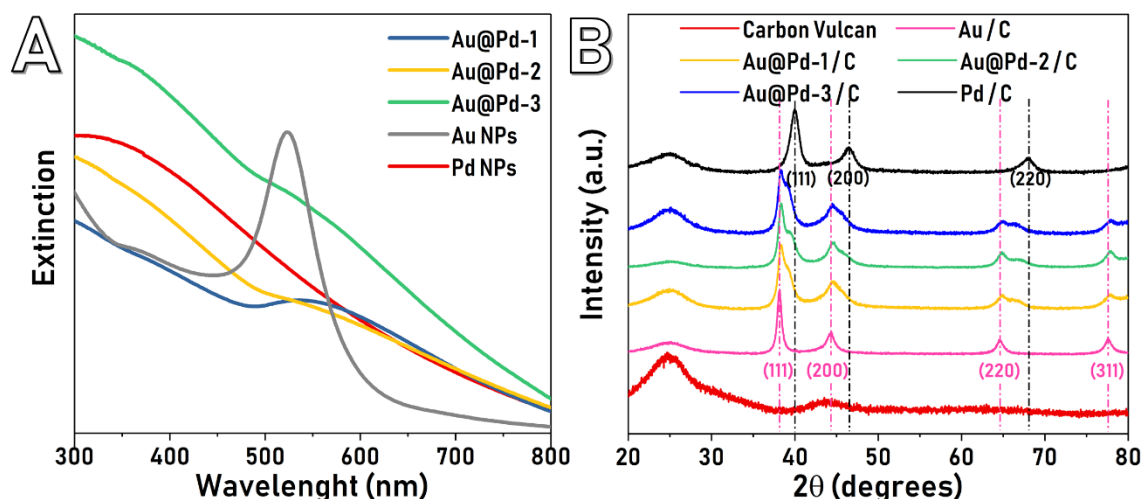
Figure 24. (A) UV-Vis extinction spectra for Au@Pd-1 (blue), Au@Pd-2 (yellow), Au@Pd-3 (green), Au NPs (grey) and Pd NPs (red). (B) XRD patterns of Vulcan carbon (red), Au nanoparticles (pink), Au@Pd with 9.0 (yellow), 12.0 (green), 14.0 (blue) nm of shell thickness, and Pd nanoparticles (black).

After the characterization of nanomaterials, were interested in the investigation of their electrocatalytic activity with and without visible light excitation (plasmonic effects). Considering that the presence of PVP can decrease the electrical conductivity[75] and the blocking the active sites on electrocatalysts surface[76,77], a method of electrochemical cleaning was proposed based on previous studies.[75,76,78] **Figure 25A-E** shows the cyclic voltammograms for the electrochemical cleaning of the electrocatalysts, where we present the first and the last cycles for each scan rate treatment. During the first potential treatment, at scan rate of 100 mVs^{-1}, the hydrogen region was observed together with a decrease of the peak at 1V (vs RHE). This is probably related to the removal of impurities from the surface, which was associated to slight increase of the PdO reduction peak.[78] Then, 10 cyclic voltammograms were performed to confirm the profile stabilization. In the final step, 3 cyclic voltammograms were recorded and compared with

the oxidation profiles. In **Figure 25F** three regions can be observed: the desorption/adsorption hydrogen region (0.05 – 0.5V), the electrical double layer regions (0.5-0.7V) and the Pd oxidation-reduction process (0.8-1.2V). These features are in agreement with the PVP removal.[79,80]

Figure 25. Cyclic voltammograms for Au@Pd-1/C (A), Au@Pd-2/C (B), Au@Pd-3/C (C), Au/C (D), and Pd/C (E) recorded in 1 mol L^{-1} KOH electrolyte during electrochemical cleaning, at scan rate 100 mV s^{-1} (20 cycles - orange line), 50 mV s^{-1} (10 cycles -green line) and 20 mV s^{-1} (3 cycles - blue line). The first and the last CV for each step of potential treatment are shown. (F) The isolated CV for all materials recorded at 20 mV s^{-1} used for electrocatalysts profile characterization after electrochemical cleaning. The experiments were carried out in a N_2 -saturated electrolyte and room temperature (25 ± 2°C)

In the next step, the electrocatalysts were evaluated for methanol oxidation reaction (MOR) and CO oxidation in absence and presence of green light irradiation (532 nm – 200 mW of maximum total source intensity), as showed in **Figure 26A-E**. The obtained oxidation currents were normalized by Pd and Au loading (for the Au/C)[81]. For

the MOR, it is very common to give voltammograms with two oxidation peaks, the forward peak related to the fresh methanol molecule oxidation and the backward peak that can be associated to incompletely oxidized methanol molecule or intermediates of the oxidation reaction.[82] This behavior was observed in our voltammograms.
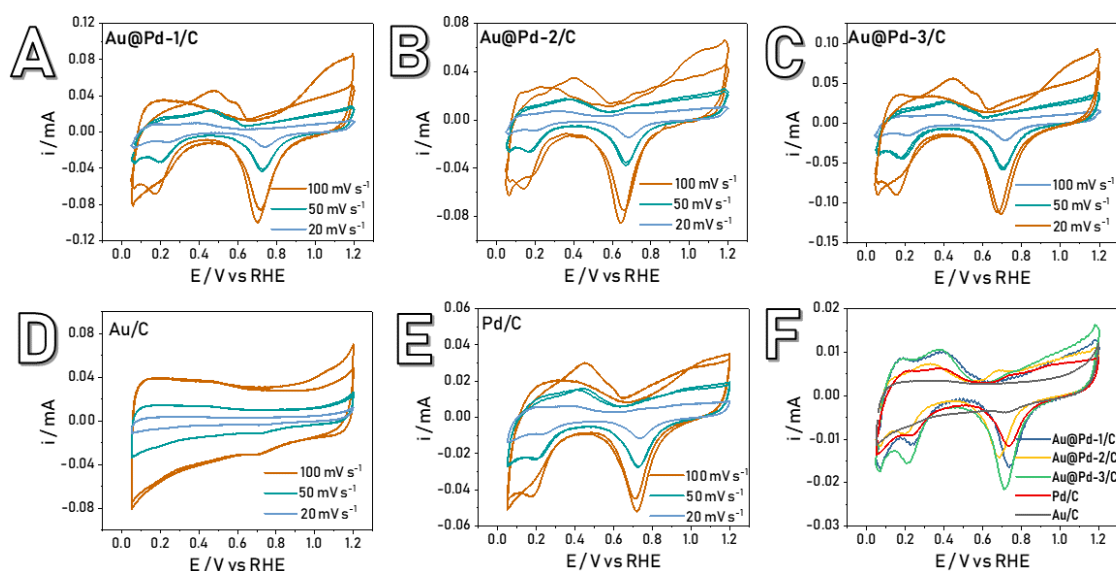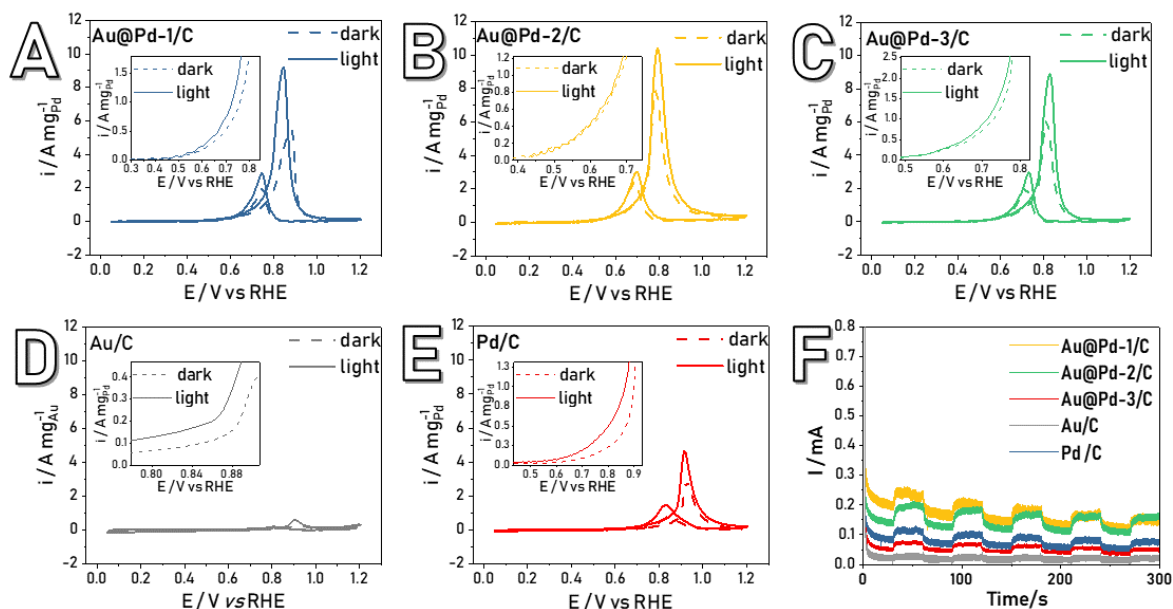

Figure 26. Cyclic voltamograms for Au@Pd-1/C (A), Au@Pd-2/C (B), Au@Pd-3/C (C), Au/C (D), and Pd/C (E) recorded in 1 mol L^{-1} KOH + 1 mol L^{-1} CH_3OH electrolyte at scan rate 20 mV s-1, without (dash line) and with (solid line) light green (532 nm) illumination. I-t curve of photocurrent response by chronoamperometry at 0.7 V (vs RHE) 0 in 1 mol L^{-1} KOH + 1 mol L^{-1} CH_3CHO electrolyte of the electrocatalysts. All the experiments were performed in a N_2 -saturated electrolyte and room temperature (25 ± 2°C). A clear increase in current densities were detected under 532 nm light (plasmonic) excitation.

It is possible to observe from the insets see that the all Au@Pd/C electrocatalysts presented onset potential for MOR lower than Pd/C and Au/C. The green light irradiation has almost no effect over this parameter, in agreement with previous studies on small molecules oxidation.[82–84] However, the green light excitation increases the oxidation

current peak for all samples. The illuminated Au@Pd-2/C exhibits the highest mass activity with a 2.5-folds increase relative to Pd/C (10.45 A mg Pd^{-1} vs 4.74 A mg Pd^{-1}). Considering the Pd-based materials, in particularly Au@Pd-3, which has almost the same size than Pd/C (61.9±3 nm and 62.1±3.9 nm, respectively) a mass activity for MOR was 2-folds higher than Pd/C. Therefore, we can suggest that the improved activity of the Au@Pd/C electrocatalysts is related to the presence of Au as the core, in which the plasmonic excitation contribute to improve the MOR activity at the Pd surfaces.[82]

The ratio of forward current (I_f) and backward current (I_b) was also calculated from the **Figure 26A-E**, and are listed in **Table 4**. This parameter is important to the poisoning tolerance of the electrocatalysts towards CO and other intermediate carbonaceous species from the methanol oxidation such as formaldehyde and formic acid. Therefore, a high value of I_f/I_b ratio indicates an effective methanol oxidation reaction with low formation of intermediates or unreacted methanol molecules.

Table 4. I_f/I_b ratio and mass specific (MA) parameters of the studied electrocatalysts towards the MOR.

Electrocatalyst	Dark		Light	
	I_f/I_b	MA (A mg$_{Pd}$$^{-1}$)	I_f/I_b	MA (A mg$_{Pd}$$^{-1}$)
Au@Pd-1/C	2.65	5.49	3.19	9.35
Au@Pd-2/C	3.28	7.79	3.47	10.45
Au@Pd-3/C	2.94	6.06	3	8.95
Au/C*	3.33	0.4	2.8	0.59
Pd/C	3.67	2.9	3.22	4.74

*[MA]= A mg$_{Au}$$^{-1}$

The green light irradiation had a positive effect improving the capability for anti-CO poisoning as illustrated by the increase of the I_f/I_b for all samples. The Au@Pd-2/C sample under light excitation (I_f/I_b = 4) presented the highest ratio among Au@Pd/C materials. The great activity toward MOR and tolerance towards CO and oxidation intermediates poisoning exhibited by Au@Pd/C can be associated to two main factors: (i) the electronic interaction between Au core and Pd shell that can avoid the poisoning-intermediates releasing the Pd active sites for the methanol molecules due to d-band shift [85,86]; (ii) the favoring of the PdO reduction to Pd, making the active sites available at more positive potentials for methanol/intermediate oxidation in the backward scan.[87] These affirmations are in agreement with a weaker effect of the illumination in Pd/C compared to Au@Pd/C samples. This agrees with the SPR-enhanced eletrocatalytic activity as promoted from the Au cores.

To further evaluate of the photo-enhanced effect on the MOR, the chronoamperometry experiments at constant potential of 0.7 V were conducted under on-off irradiation using green light (532 nm) as the irradiation source. The **Figure 26F** displays a reversible current response behavior in on-off illumination conditions for all nanostructures. In additional, the Au@Pd-2/C and Au@Pd-3/C gave a superior current during the short experiment compared to Pd/C, indicating, a good tolerance to intermediates of reaction as observed in the CVs for methanol and CO oxidation reactions. Here, it is plausible that the increased response under visible light excitation occurs as a result of the transfer of SPR-excited hot electrons from Au to Pd, increasing its activity.[88,89]

In order to get more insights into the CO poisoning tolerance, cyclic voltamograms were performed in the same electrochemical conditions employed in the MOR from the CO adlayer on the catalyst surface. **Figure 27** displays the CO stripping

voltammograms under absence and presence of green light illumination. The CO oxidation peak potential was very similar for all prepared electrocatalysts, with a slight shift for lower potential values under green light illumination with the increase of Pd content in the material. Additionally, the defined adsorption-desorption hydrogen region after the consecutive cycles after CO stripping could be detected, indicating an effective release of the Pd active sites and great anti-CO poisoning capability of the materials. The PdO reduction charge was used [90] to calculate the electrochemical activity area for Pd-based electrocatalysts and so the PdO reduction charge under absence and presence of green light illumination was determined to comparison. The PdO stripping is used to estimate the ECSA[91] of Pd according to equation:

$$ECSA = {Q_O}/{0.42 \ x \ m_{Pd}}$$

where $Q_{o \ is}$ the charge of the PdO reduction, 0.42 (in mC cm^{-2}) is the charge related to oxygen monolayer chemisorption on the Pd electrocatalyst, and m_{Pd} is the Pd loading on the carbon glassy substrate.
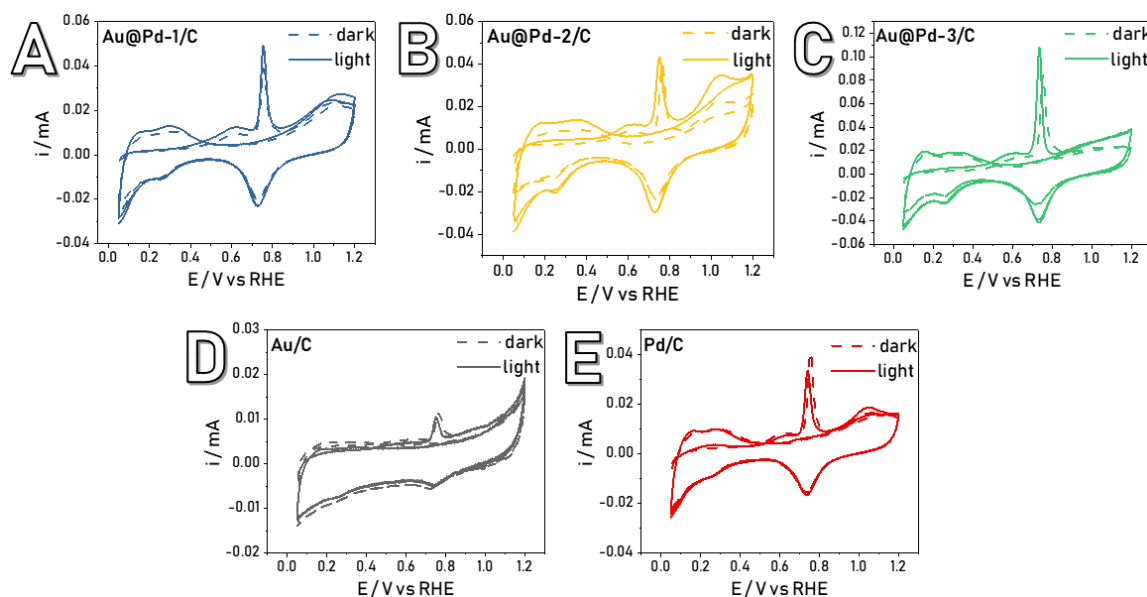
Figure 27. CO stripping voltammetry for Au@Pd-1/C (A), Au@Pd-2/C (B), Au@Pd-3/C (C), Au/C (D), and Pd/C (E) materials recorded in 1 mol L^{-1} KOH electrolyte at scan rate 20 mV s-1, without (dash line) and with (solid line) light green (532 nm) illumination. Before experiment, CO was adsorbed during 5 minutes at 0.1 V (vs RHE) on electrode and then N$_2$ was purged for 25 minutes to eliminate the CO in electrolyte. Scan rate: 20 mV s^{-1}. Room temperature (25 ±2°C).

From the CO stripping voltammetries, it is possible to see that the CO oxidation charge increase and CO oxidation peak presents a slight shift to less positive potentials upon green light illumination and as the Pd shell became thicker.[87] This effect is not observed for Pd/C electrocatalysts. It is discussed[72–74] that the improved catalytic activity in Au@Pd core-shell nanostructures is related to the transfer of SPR-excited charge carriers from Au to the Pd, which can further participate in the electrochemical transformations[89] in which Au can transfer electrons to Pd and facilitate the hot electrons excitation in core-shell nanostructures. This can, in fact, enhance electrocatalytic activity and increase the electrochemical active area (ECSA), as observed in the **Table 5**.

Table 5. Electrochemical parameters about electrochemical activity area.

Electrocatalyst	Pd mass on electrode (μg)*	PdO charge(uC)		ECSA (m² g⁻¹)	
		Dark	Light	Dark	Light
Au@Pd-1/C	0.187	120	120	151	151
Au@Pd-2/C	0.137	118	158	201	269
Au@Pd-3/C	0.226	200	223	209	233
Pd /C	0.206	99.4	95.2	113	109
Au/C	0.175	11.5	11.5	8.41	8.41

*Pd mass used for all electrochemical experiments, determined by ICP-OES.

Based on these results, we suggest a mechanism (**Figure 28**) for the plasmonic photoelectrooxidation of methanol based in the plasmon-enhanced anti-CO poisoning capability of the Au@Pd nanostructures and charge transfer of SPR-excited charge carriers from Au to Pd, which can further participate in redox processes.
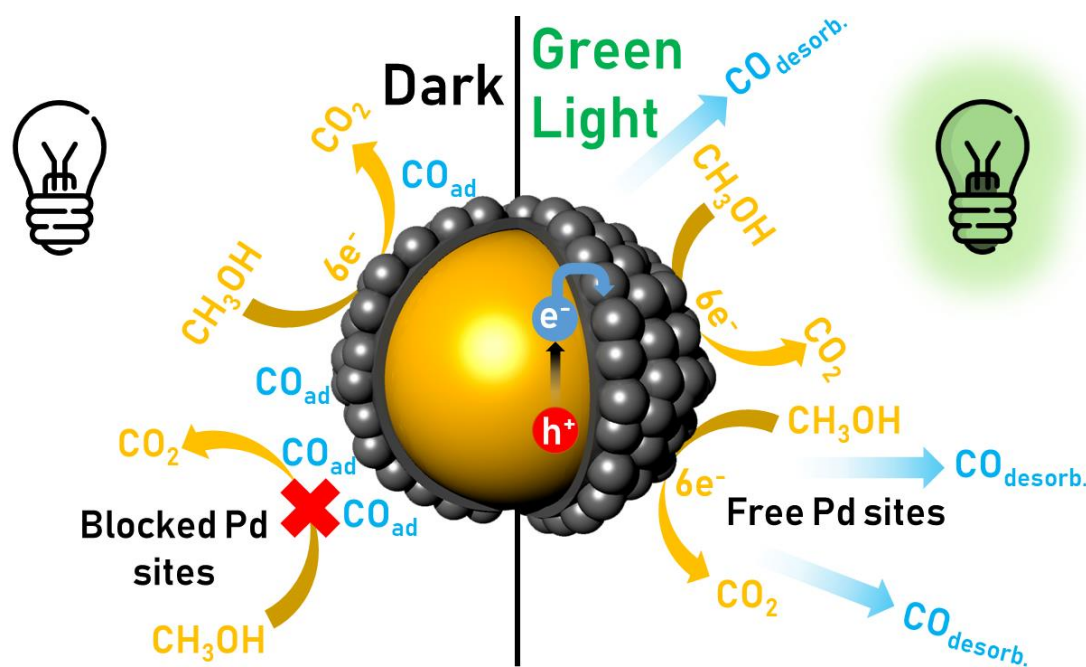
Figure 28. Schematic illustration of the proposed mechanism for the plasmon-enhanced photoelectrooxidation of methanol in Au@Pd materials.

5   Conclusions

In this work, we developed facile and environmentally friendly strategies for the synthesis of two kinds of nanostructures having branched morphologies: *i*) monometallic Au nanodendrites and nanourchins and *ii*) Au@Pd core-shell nanoparticles. These materials were employed as model systems in order to understand how catalytic and electrocatalytic processes can be accelerated or enhanced as a result of plasmonic (SPR) excitation in Au. In this case, the Au nanodendrites and nanourchins are attractive as the tips or branches at their surface enable a higher concentration of electric fields due to SPR excitation relative to rounded nanoparticles. Moreover, the junctions between the branches enable the generation of electromagnetic hot spots, which can further contribute to plasmonic catalytic activities. The Au nanodendrites and nanourchins were studies towards the SPR-mediated oxidation of p-aminothiophenol and the liquid phase oxidation benzylamine as a function of their surface morphology. Our results indicated that superior performances could be achieved relative to rounded (conventional) Au nanoparticles. However, our data indicates that, in liquid phase transformations, stability of the nanodendrites and nanourchins under the reaction conditions played an important role over the detected activities and must be properly addressed in the field of plasmonic catalysis. In the case of Au@Pd materials, we controlled the thickness of the Pd-based shells and investigated their performance towards the plasmonically-enhanced methanol oxidation reaction. We observed that improved performances relative to Au/C and Pd/C could be achieved under visible light excitation. The nanostructures were also tolerant to poisoning by intermediates under SPR excitation and that there is an optimum thickness of the Pd shell for the optimization of the performances. We believe the results described

herein can shed important insights into the design of monometallic and bimetallic nanomaterials for applications in catalysis and electrocatalysis.

6 References

1. Baughman, R. H., Zakhidov, A. A. & Heer, W. A. De. Carbon Nanotubes — the Route Toward Applications. **297,** 787–793 (2002).

2. Singh, V., Joung, D., Zhai, L. & Das, S. Progress in Materials Science Graphene based materials : Past , present and future. *Prog. Mater. Sci.* **56,** 1178–1271 (2011).

3. Tian, B. *et al.* Coaxial silicon nanowires as solar cells and nanoelectronic power sources. **449,** 885–890 (2007).

4. Yao, Y. *et al.* Interconnected Silicon Hollow Nanospheres for Lithium-Ion Battery Anodes with Long Cycle Life. 2949–2954 (2011). doi:10.1021/nl201470j

5. Chen, X. & Mao, S. S. Titanium Dioxide Nanomaterials : Synthesis , Properties , Modifications , and Applications. (2007). doi:10.1021/cr0500535

6. Rodrigues, T. S. *et al.* Controlling Reduction Kinetics in the Galvanic Replacement Involving Metal Oxides Templates : Elucidating the Formation of Bimetallic Bowls , Rattles , and Dendrites from Cu 2 O Spheres. **1700175,** 1–9 (2018).

7. Xia, Y., Xiong, Y., Lim, B. & Skrabalak, S. E. Shape-controlled synthesis of metal nanocrystals: Simple chemistry meets complex physics? *Angew. Chemie - Int. Ed.* **48,** 60–103 (2009).

8. Geonmonond, R. S., Silva, A. G. M. D. A. & Camargo, P. H. C. Controlled synthesis of noble metal nanomaterials : motivation , principles , and opportunities in nanocatalysis. **90,** 719–744 (2018).

9. Nanocomposite. *IUPAC Compend. Chem. Terminol.* **1801,** 7243 (2014).

10. Philippot, K. & Serp, P. Concepts in Nanocatalysis. *Nanomater. Catal. First Ed.* 1–54 (2012). doi:10.1002/9783527656875.ch1

11. Aiken, J. D. & Finke, R. G. A review of modern transition-metal nanoclusters: their synthesis, characterization, and applications in catalysis. *J. Mol. Catal. A Chem.* **145,** 1–44 (1999).

12. Xia, Y., Gilroy, K. D., Peng, H. C. & Xia, X. Seed-Mediated Growth of Colloidal Metal Nanocrystals. *Angew. Chemie - Int. Ed.* **56,** 60–95 (2017).

13. Picraux, S. T. Nanotechnology. (2018). Available at: https://www.britannica.com/technology/nanotechnology/Nanofabrication. (Accessed: 12th August 2018)

14. Schmitz-Antoniak, C. X-ray absorption spectroscopy on magnetic nanoscale systems for modern applications. *Reports Prog. Phys.* **78,** (2015).

15. Xiong, Y. & Lu, X. *Metallic nanostructures: From controlled synthesis to applications*. *Metallic Nanostructures: From Controlled Synthesis to Applications* (2015). doi:10.1007/978-3-319-11304-3

16. Ruditskiy, A., Peng, H. & Xia, Y. {Shape-Controlled} Metal Nanocrystals for Heterogeneous Catalysis. **7,** 1–22 (2015).

17. Cao, S., Tao, F. F., Tang, Y., Li, Y. & Yu, J. Size- and shape-dependent catalytic performances of oxidation and reduction reactions on nanocatalysts. *Chem. Soc. Rev.* **45,** 4747–4765 (2016).

18. Gawande, M. B. *et al.* Core–shell nanoparticles: synthesis and applications in catalysis and electrocatalysis. *Chem. Soc. Rev.* **44,** 7540–7590 (2015).

19. Witte, J. d-Band Theory. Available at: https://sites.google.com/site/orrcatalysiswithptbasedcsnps/home/d-band-theory. (Accessed: 30th October 2018)

20. Da Silva, A. G. M., Rodrigues, T. S., Haigh, S. J. & Camargo, P. H. C. Galvanic replacement reaction: Recent developments for engineering metal nanostructures towards catalytic applications. *Chem. Commun.* **53,** 7135–7148 (2017).

21. Sanchez-Gaytan, B. L. *et al.* Spiky gold nanoshells: Synthesis and enhanced scattering properties. *J. Phys. Chem. C* **116,** 10318–10324 (2012).

22. Pedireddy, S. *et al.* Synthesis of spiky Ag-Au octahedral nanoparticles and their tunable optical properties. *J. Phys. Chem. C* **117,** 16640–16649 (2013).

23. Jana, D. *et al.* Surface Enhanced Raman Spectroscopy of a Au@Au Core-Shell Structure Containing a Spiky Shell. *J. Phys. Chem. C* acs.jpcc.6b02135 (2016). doi:10.1021/acs.jpcc.6b02135

24. Lee, Y. & Park, T. G. Facile fabrication of branched gold nanoparticles by reductive hydroxyphenol derivatives. *Langmuir* **27,** 2965–2971 (2011).

25. Back, S. & Jung, Y. Importance of Ligand Effects Breaking the Scaling Relation for Core-Shell Oxygen Reduction Catalysts. *ChemCatChem* **9,** 3173–3179 (2017).

26. Ozoemena, K. I. Nanostructured platinum-free electrocatalysts in alkaline direct alcohol fuel cells: Catalyst design, principles and applications. *RSC Adv.* **6,** 89523–89550 (2016).

27. Antolini, E. Palladium in fuel cell catalysis. *Energy Environ. Sci.* **2,** 915–931 (2009).

28. Brouzgou, A., Song, S. Q. & Tsiakaras, P. Low and non-platinum electrocatalysts for PEMFCs: Current status, challenges and prospects. *Appl. Catal. B Environ.* **127,** 371–388 (2012).

29. Stewart, M. E. *et al.* Nanostructured plasmonic sensors. *Chem. Rev.* **108,** 494–521 (2008).

30. Atwater, H. A. & Polman, A. Plasmonics for improved photovoltaic devices. *Nat. Mater.* **9,** 865–865 (2010).

31. Christopher, P., Xin, H. & Linic, S. Visible-light-enhanced catalytic oxidation reactions on plasmonic silver nanostructures. *Nat. Chem.* **3,** 467–472 (2011).

32. Baffou, G. & Quidant, R. Nanoplasmonics for chemistry. *Chem. Soc. Rev.* **43,** 3898–3907 (2014).

33. Linic, S., Aslam, U., Boerigter, C. & Morabito, M. Photochemical transformations on plasmonic metal nanoparticles. *Nat. Mater.* **14,** 567–576 (2015).

34. Willets, K. A. & Van Duyne, R. P. Localized Surface Plasmon Resonance Spectroscopy and Sensing. *Annu. Rev. Phys. Chem.* **58,** 267–297 (2007).

35. Kelly, K. L., Coronado, E., Zhao, L. L. & Schatz, G. C. The Optical Properties of Metal Nanoparticles: The Influence of Size, Shape, and Dielectric Environment. *J. Phys. Chem. B* **107,** 668–677 (2003).

36. Lu, X., Rycenga, M., Skrabalak, S. E., Wiley, B. & Xia, Y. Chemical Synthesis of Novel Plasmonic Nanoparticles. *Annu. Rev. Phys. Chem.* **60,** 167–192 (2009).

37. Schlücker, S. Surface-enhanced raman spectroscopy: Concepts and chemical

applications. *Angew. Chemie - Int. Ed.* **53,** 4756–4795 (2014).

38. Kale, M. J., Avanesian, T. & Christopher, P. Direct photocatalysis by plasmonic nanostructures. *ACS Catal.* **4,** 116–128 (2014).

39. Zhang, Y., Aslan, K. & Previte, M. J. R. Metal-enhanced superoxide generation : A consequence of plasmon-enhanced triplet yields. 3–5 (2007). doi:10.1063/1.2753718

40. Mukherjee, S. *et al.* Hot electrons do the impossible: Plasmon-induced dissociation of H2on Au. *Nano Lett.* **13,** 240–247 (2013).

41. Li, Y., Zhang, P., Duan, J., Ai, S. & Li, H. One-step seeded growth of monodisperse, quasi-spherical, Tris-stabilized gold nanocrystals with sizes from 17 to 325 nm. *CrystEngComm* **19,** 318–324 (2017).

42. Geonmonond, R. S. *et al.* Marrying SPR excitation and metal-support interactions: Unravelling the contribution of active surface species in plasmonic catalysis. *Nanoscale* **10,** 8560–8568 (2018).

43. Perrault, S. D. & Chan, W. C. W. Synthesis and Surface Modification of Highly Monodispersed, Spherical Gold Nanoparticles of 50-200 (vol 131, pg 17042, 2009). *J. Am. Chem. Soc.* **132,** 11824 (2010).

44. Sirajuddin *et al.* The formation of gold nanoparticles using hydroquinone as a reducing agent through a localized pH change upon addition of NaOH to a solution of HAuCl4. *Colloids Surfaces A Physicochem. Eng. Asp.* **370,** 35–41 (2010).

45. Kumar, D., Mutreja, I. & Sykes, P. Seed mediated synthesis of highly mono-dispersed gold nanoparticles in the presence of hydroquinone. *Nanotechnology* **27,**

1–14 (2016).

46. Li, J. *et al.* Controllable synthesis of stable urchin-like gold nanoparticles using hydroquinone to tune the reactivity of gold chloride. *J. Phys. Chem. C* **115,** 3630–3637 (2011).

47. Da Silva, A. G. M. *et al.* Controlling Size, Morphology, and Surface Composition of AgAu Nanodendrites in 15 s for Improved Environmental Catalysis under Low Metal Loadings. *ACS Appl. Mater. Interfaces* **7,** 25624–25632 (2015).

48. Ji, X. *et al.* Size control of gold nanocrystals in citrate reduction: The third role of citrate. *J. Am. Chem. Soc.* **129,** 13939–13948 (2007).

49. Zhu, M. *et al.* Branched au nanostructures enriched with a uniform facet: Facile synthesis and catalytic performances. *Sci. Rep.* **4,** (2014).

50. Hughes, M. D. *et al.* Tunable gold catalysts for selective hydrocarbon oxidation under mild conditions. *Nature* **437,** 1132–1135 (2005).

51. Haruta, M. Catalysis: Gold rush. *Nature* **437,** 1098–1099 (2005).

52. Min, B. K. & Friend, C. M. Heterogeneous gold-based catalysis for green chemistry: Low-temperature CO oxidation and propene oxidation. *Chem. Rev.* **107,** 2709–2724 (2007).

53. Rodrigues, T. S., Da Silva, A. G. M., De Moura, A. B. L., Geonmonond, R. S. & Camargo, P. H. C. AgAu nanotubes: Investigating the effect of surface morphologies and optical properties over applications in catalysis and photocatalysis. *J. Braz. Chem. Soc.* **28,** 1630–1638 (2017).

54. Quiroz, J. *et al.* Controlling Reaction Selectivity over Hybrid Plasmonic Nanocatalysts. *Nano Lett.* **18,** acs.nanolett.8b03499 (2018).

55. Da Silva, A. G. M. *et al.* The Fault in Their Shapes: Investigating the Surface-Plasmon-Resonance-Mediated Catalytic Activities of Silver Quasi-Spheres, Cubes, Triangular Prisms, and Wires. *Langmuir* **31,** 10272–10278 (2015).

56. Huang, Y. F. *et al.* Surface-enhanced Raman spectroscopic study of p-aminothiophenol. *Phys. Chem. Chem. Phys.* **14,** 8485–8497 (2012).

57. Baffou, G. & Quidant, R. Nanoplasmonics for chemistry. *Chem. Soc. Rev.* **43,** 3898 (2014).

58. Huang, Y. F. *et al.* Activation of oxygen on gold and silver nanoparticles assisted by surface plasmon resonances. *Angew. Chemie - Int. Ed.* **53,** 2353–2357 (2014).

59. Fang, Y., Li, Y., Xu, H. & Sun, M. Ascertaining p, p'-dimercaptoazobenzene produced from p-aminothiophenol by selective catalytic coupling reaction on silver nanoparticles. *Langmuir* **26,** 7737–7746 (2010).

60. Sun, M., Zhang, Z., Zheng, H. & Xu, H. In-situ plasmon-driven chemical reactions revealed by high vacuum tip-enhanced Raman spectroscopy. *Sci. Rep.* **2,** 2–5 (2012).

61. Liang, H., Li, Z. P., Wang, W., Wu, Y. & Xu, H. Highly surface-roughened 'flower-like' silver nanoparticles for extremely sensitive substrates of surface-enhanced Raman scattering. *Adv. Mater.* **21,** 4614–4618 (2009).

62. Li, M. *et al.* Design of SERS nanoprobes for Raman imaging: materials, critical factors and architectures. *Acta Pharm. Sin. B* **8,** 381–389 (2018).

63. Li, A. & Li, S. Large-volume hot spots in gold spiky nanoparticle dimers for high-performance surface-enhanced spectroscopy. *Nanoscale* **6,** 12921–12928 (2014).

64. Susut, C., Nguyen, T. D., Chapman, G. B. & Tong, Y. Y. Shape and size stability of Pt nanoparticles for MeOH electro-oxidation. *Electrochim. Acta* **53,** 6135–6142 (2008).

65. González, A. L., Noguez, C., Beránek, J. & Barnard, A. S. Size, shape, stability, and color of plasmonic silver nanoparticles. *J. Phys. Chem. C* **118,** 9128–9136 (2014).

66. Jain, P. K., Lee, K. S., El-Sayed, I. H. & El-Sayed, M. A. Calculated absorption and scattering properties of gold nanoparticles of different size, shape, and composition: Applications in biological imaging and biomedicine. *J. Phys. Chem. B* **110,** 7238–7248 (2006).

67. da Silva, A. G. M. *et al.* Pd-based nanoflowers catalysts: controlling size, composition, and structures for the 4-nitrophenol reduction and BTX oxidation reactions. *J. Mater. Sci.* **51,** 603–614 (2015).

68. Xu, J. *et al.* Synthesis and catalytic properties of Au-Pd nanoflowers. *ACS Nano* **5,** 6119–6127 (2011).

69. Lim, B., Jiang, M., Yu, T., Camargo, P. H. C. & Xia, Y. Nucleation and growth mechanisms for Pd-Pt bimetallic nanodendrites and their electrocatalytic properties. *Nano Res.* **3,** 69–80 (2010).

70. Zhang, C., Chen, B.-Q., Li, Z.-Y., Xia, Y. & Chen, Y.-G. Surface Plasmon Resonance in Bimetallic Core–Shell Nanoparticles. *J. Phys. Chem. C* **119,** 16836–16845 (2015).

71. Wu, J. *et al.* Surface lattice-engineered bimetallic nanoparticles and their catalytic

properties. 8066–8074 (2012). doi:10.1039/c2cs35189g

72. Kuo, C. H. *et al.* The effect of lattice strain on the catalytic properties of Pd nanocrystals. *ChemSusChem* **6,** 1993–2000 (2013).

73. Chen, D., Li, C., Liu, H., Ye, F. & Yang, J. Core-shell Au@Pd nanoparticles with enhanced catalytic activity for oxygen reduction reaction via core-shell Au@Ag/Pd constructions. *Sci. Rep.* **5,** 1–9 (2015).

74. Celorrio, V. *et al.* Strain Effects on the Oxidation of CO and HCOOH on Au-Pd Core-Shell Nanoparticles. *ACS Catal.* **7,** 1673–1680 (2017).

75. Arjona, N. *et al.* Electrocatalytic activity of well-defined and homogeneous cubic-shaped Pd nanoparticles. *J. Mater. Chem. A* **1,** 15524–15529 (2013).

76. Yang, H., Tang, Y. & Zou, S. Electrochemical removal of surfactants from Pt nanocubes. *Electrochem. commun.* **38,** 134–137 (2014).

77. Su, N. *et al.* The facile synthesis of single crystalline palladium arrow-headed tripods and their application in formic acid electro-oxidation. *Chem. Commun.* **51,** 7195–7198 (2015).

78. Martins, C. A. *et al.* Agglomeration and Cleaning of Carbon Supported Palladium Nanoparticles in Electrochemical Environment. *Electrocatalysis* **5,** 204–212 (2014).

79. Gong, K., Vukmirovic, M. B., Ma, C., Zhu, Y. & Adzic, R. R. Synthesis and catalytic activity of Pt monolayer on Pd tetrahedral nanocrystals with CO-adsorption-induced removal of surfactants. *J. Safety Res.* **40,** 21–4 (2009).

80. Liu, Z. *et al.* Carbon nanotube/raspberry hollow Pd nanosphere hybrids for

methanol, ethanol, and formic acid electro-oxidation in alkaline media. *J. Colloid Interface Sci.* **351,** 233–238 (2010).

81. Zanata, C. R. *et al.* Estimating the time-dependent performance of nanocatalysts in fuel cells based on a cost-normalization approach. *J. Braz. Chem. Soc.* **27,** 1980–1988 (2016).

82. Tan, Q. *et al.* Highly efficient and stable nonplatinum anode catalyst with Au@Pd core-shell nanostructures for methanol electrooxidation. *J. Catal.* **295,** 217–222 (2012).

83. Wang, C. *et al.* Direct Plasmon-Accelerated Electrochemical Reaction on Gold Nanoparticles. *ACS Nano* **11,** 5897–5905 (2017).

84. Wang, Q. *et al.* Plasmonic-induced inhibition and enhancement of the electrocatalytic activity of Pd-Au hetero-nanoraspberries for ethanol oxidation. *J. Power Sources* **316,** 29–36 (2016).

85. Wang, H., Sun, Z., Yang, Y. & Su, D. The growth and enhanced catalytic performance of Au@Pd core-shell nanodendrites. *Nanoscale* **5,** 139–142 (2013).

86. Zhao, Y. *et al.* Colloidal Synthesis of Au@Pd Core–Shell Nanorods with Tunable Dimensions and Enhanced Electrocatalytic Activities. *Top. Catal.* **61,** 949–957 (2018).

87. Kelly, C. H. W. *et al.* Understanding the Effect of Au in Au-Pd Bimetallic Nanocrystals on the Electrocatalysis of the Methanol Oxidation Reaction. *J. Phys. Chem. C* **122,** 21718–21723 (2018).

88. Yang, H. *et al.* Quantitative Detection of Photothermal and Photoelectrocatalytic

Effects Induced by SPR from Au@Pt Nanoparticles. *Angew. Chemie - Int. Ed.* **54,** 11462–11466 (2015).

89.   Yang, H. *et al.* Surface plasmon resonance promoted photoelectrocatalyst by visible light from Au core Pd shell Pt cluster nanoparticles. *Electrochim. Acta* **209,** 591–598 (2016).

90.   Lukaszewski, M., Soszko, M. & Czerwiński, A. Electrochemical methods of real surface area determination of noble metal electrodes - an overview. *Int. J. Electrochem. Sci.* **11,** 4442–4469 (2016).

91.   Da, Z. *et al.* From Moldy Orange Waste to Natural Reductant and Catalyst Support: Active Palladium/Biomass-Derived Carbonaceous Hybrids for Promoted Methanol Electro-Oxidation. *ChemElectroChem* **4,** 1372–1377 (2017).

CURRICULUM VITAE

Vitor Renato Ribeiro Silveira

Born 2 December 1992 in Espírito Santo, Brazil.

EDUCATION

Universidade de São Paulo, São Paulo, Brazil.

M. Sc. in Chemistry, ongoing.

Universidade Federal do Espírito Santo, Espírito Santo, Brazil.

B. Sc. in Chemistry with Specialization in Petroleum Chemistry, 2016

EEEM Ormanda Gonçalves, Espírito Santo, Brazil.

High School, 2010

OCCUPATION

M. Sc. Student

Universidade de São Paulo, São Paulo, Brazil.

CNPQ Fellowship, 09/2018 – 01/2019.

RESEARCH EXPERIENCE

Graduate Research Fellow

Universidade de São Paulo, São Paulo, Brazil.

(Advisor: Pedro H. C. Camargo)

- *Worked in synthesis of nanomaterials with controlled properties (size, shape, composition, architecture) for application in heterogeneous plasmon-mediated photocatalysis and photoelectrocatalysis.*

Undergraduate Research Fellow

Universidade Federal do Espírito Santo, Espírito Santo, Brazil.

(Advisor: Carlos A. C. Passos)

- *Worked in the development of new synthetic routes to obtain superconducting ceramics of high temperature based in samarium, barium and copper.*

TEACHING EXPERIENCE

Graduate monitor

Universidade de São Paulo, São Paulo, Brazil.

- Analytical Chemistry

Activities included: Answering students questions, conducting lab practices, and correcting homeworks.

Graduate monitor

Universidade Federal do Espírito Santo, Espírito Santo, Brazil.

- Inorganic Chemistry

Activities included: answering students questions, delivering classes, conducting lab practices, and elaborating/correcting homeworks.

Chemistry teacher (volunteer work)

Projeto Educacional Compartilhando Saberes (PROEX – UFES) - Universidade Federal do Espírito Santo, Espírito Santo, Brazil.

- *Worked teaching Chemistry as a volunteer in a sucessful social project which aimed the approval of low-income students on the college admission exam.*